
Background Studies for the ECHO Experiment

DISSERTATION

der Mathematisch-Naturwissenschaftlichen Fakultät
der Eberhard Karls Universität Tübingen
zur Erlangung des Grades eines
Doktors der Naturwissenschaften
(Dr. rer. nat.)

vorgelegt von
ALEXANDER SEBASTIAN GÖGGELMANN
geb. Ziegenbein
aus Herten

Tübingen 2022

Gedruckt mit Genehmigung der Mathematisch-Naturwissenschaftlichen
Fakultät der Eberhard Karls Universität Tübingen.

Tag der mündlichen Qualifikation:	21.06.2022
Dekan:	Prof. Dr. Thilo Stehle
1. Berichterstatter:	Prof. Dr. Josef Jochum
2. Berichterstatter:	Prof. Dr. Tobias Lachenmaier

Zusammenfassung

Die Zielsetzung des “Elektron Capture ^{163}Ho ” (ECHO) Experiments ist die Bestimmung der effektiven Elektroneneutrino­masse. Hierzu wird das Spektrum des ^{163}Ho Elektroneinfangs (EC) analysiert, welches von metallischen magnetischen Kalorimetern (MMCs) aufgenommen wird. Die MMCs sind nach einem gepixelten Schema angeordnet und mit ^{163}Ho implantiert. Am stärksten wird die Endpunktregion um $Q_{\text{EC}} \approx 2.8\text{ keV}$ des ^{163}Ho EC Spektrums von der effektiven Neutrino­masse beeinflusst. Jedoch ist der Anteil an Ereignissen in der relevanten Region (ROI), 10 eV unterhalb Q_{EC} , mit einer Größenordnung von 10^{-9} sehr klein. Auch mit je einer ^{163}Ho Konzentration mit einer Aktivität von 1 Bq in jedem MMC Pixel, führt dies ebenfalls nur zu einer sehr kleinen Zählrate in der Größenordnung von 10^{-4} Zählungen $\text{Tag}^{-1}\text{ Pixel}^{-1}$, weshalb sich die Beschreibung der Endpunktregion auf eine präzise Kenntnis des erwarteten ^{163}Ho EC Spektrum sowie des Untergrunds stützen muss.

In dieser Arbeit wird der erwartete Untergrund diskutiert, welcher sich aus kosmischen Myonen und natürlich vorkommenden Radionukliden zusammensetzt. Letztere befinden sich in der nahen Umgebung der Detektorpixel. Dazu wurden mithilfe des GEANT4-Frameworks Monte-Carlo-Simulationen durchgeführt, um die Energiedeposition in den MMCs zu studieren. Diese Energiedeposition wird durch Myonen und durch myoninduzierte Strahlung verursacht, welche entsteht, wenn Myonen durch Materie durchqueren. Ergebnisse von Screening Messungen von Proben, die in der ersten Phase des ECHO Experiments, ECHO-1k, benutzt wurden, dienen als Grundlage der Simulationen von Radioisotopen in der Materie, die sich in der näheren Umgebung der Detektorpixel befinden.

Die Ergebnisse der Simulationen von radioaktiver Kontamination wird mit einem Untergrundspektrum verglichen, welches mit nicht-implantierten Pixeln aufgenommen wurde. Zudem wird die Simulation von myoninduziertem Untergrund mit Daten verglichen, welche in einer Messung mit einem aktiven Myonveto aufgenommen wurden. Das Veto wurde dazu um einen Kryostaten gestellt, welcher benutzt wurde, um die Detektoren zu betreiben.

Die Pulse, die mit den MMCs aufgenommen wurden, wurden einer Pulsformanalyse unterzogen, um ^{163}Ho -induzierte und vergleichbare Ereignisse, welche durch Teilchen hervorgerufen werden, die in den MMCs absorbiert werden, zu identifizieren, sowie um Ereignisse zu identifizieren, welche durch Myonen generiert wurden.

Schlagwörter: Untergrund, ECHO, Myonen, Natürliche Radioaktivität, ^{163}Ho , Pulsformanalyse

Abstract

The aim of the Electron Capture ^{163}Ho (ECHO) experiment is the determination of the effective electron neutrino mass. This should be achieved by analyzing the ^{163}Ho electron capture (EC) spectrum recorded by ^{163}Ho -implanted metallic magnetic calorimeters (MMCs) arranged in a pixelized array. The influence of the neutrino mass on the shape of the ^{163}Ho EC spectrum is strongest at the endpoint region around $Q_{\text{EC}} \approx 2.8$ keV. However, the fraction of events in the region of interest (ROI) of 10 eV below Q_{EC} is only in the order of 10^{-9} resulting in low count rates of the order of 10^{-4} counts day $^{-1}$ pixel $^{-1}$ for an activity of 1 Bq of ^{163}Ho per MMC pixel. Thus, the description of the endpoint region has to rely on the precise knowledge of the expected ^{163}Ho events and background events. The background in the ROI is aimed to be dominated by unresolved pile-up, which is expected to be in the order of $10^{-6} - 10^{-5}$ counts day $^{-1}$ pixel $^{-1}$.

In this work, the expected background caused by cosmic muons and natural occurring radionuclides located in the next surrounding of the detector arrays is discussed. For this purpose, Monte Carlo simulations based on the GEANT4 framework are performed to study the energy deposition in the MMCs due to muons and radiation produced by muons propagating through materials surrounding the detector array. Results of screening measurements of materials used in the first stage of the ECHO experiment, ECHO-1k, are used as basis for simulations of radioisotopes in materials close to the detector array.

The results of the simulations of radioactive contamination is compared with a background spectra acquired by non- ^{163}Ho -implanted pixels, while the simulation of muonic background is compared to data acquired by a measurement including an active muon veto installed around the cryostat used for the operation of the detectors.

A pulse shape analysis of pulses received by the MMCs is used to identify ^{163}Ho induced and similar events caused by particles stopped in the MMCs, and is used to identify events generated by muons.

Keywords: Background, ECHO, Muons, Natural Radioactivity, ^{163}Ho , Pulse Shape Analysis

Contents

1	Introduction	1
1.1	Neutrino Masses	1
1.1.1	Neutrino Cosmology	2
1.1.2	Direct neutrino mass measurement	2
1.2	The ECHo Experiment	3
1.2.1	Metallic Magnetic Calorimeters	4
1.2.2	Experiment Set-Up	5
1.3	Background Sources	6
1.3.1	Unresolved pile-up	6
1.3.2	Electromagnetic noise	7
1.3.3	Co-implanted isotopes	7
1.3.4	Natural occurring radionuclides	7
1.3.5	Cosmogenic muons	8
2	Objective	11
3	Monte Carlo Simulations	13
3.1	Set-Up	13
3.2	Muons	15
3.3	Natural Radionuclides	17
4	Measurements	21
4.1	Pulse Shape Analysis	21
4.2	Muonic Background – Data set (1)	25
4.3	Background Measurement - Data set (2)	29
5	Conclusion and Outlook	33

Acronyms

CMB Cosmic Microwave Background

EC electron capture

ECh_o Electron Capture ¹⁶³Holmium

MMC metallic magnetic calorimeter

ROI region of interest

SQUID superconducting quantum interference device

SSM Standard Solar Model

List of accepted papers

Göggelmann, A. *et al.* Study of muon-induced background in MMC detector arrays for the ECHo experiment. *Eur. Phys. J. C* **81**, 363 (2021).
<https://doi.org/10.1140/epjc/s10052-021-09148-y>

Göggelmann, A. *et al.* Study of naturally occurring radionuclides in the ECHo set-up. *Eur. Phys. J. C* **82**, 139 (2022).
<https://doi.org/10.1140/epjc/s10052-022-10112-7>

C. Velte *et al.* High-resolution and low-background ^{163}Ho spectrum: interpretation of the resonance tail. *Eur. Phys. J. C* **79**, 1026 (2019).
<https://doi.org/10.1140/epjc/s10052-019-7513-x>

List of not submitted manuscripts

Göggelmann, A. *et al.* A pulse shape analysis for the ECHo experiment.

Declaration of own contribution

The data analyzed in this work were received by the ECHo detectors located in Heidelberg (Germany), which were also developed and operated there [1–4].

The discussion of the Monte Carlo simulations of cosmogenic muons and natural radionuclides including the implementation and analysis are exclusively performed in this work, as well as the operation of the active muon veto and the analysis of data received by the veto system.

The pulse shape analysis described in this work was independently developed in this work, but is based on the method of template fitting used in previous work [4–6].

“C. Velte *et al.* High-resolution and low-background ^{163}Ho spectrum: interpretation of the resonance tail. *Eur. Phys. J. C* **79**, 1026 (2019)” is a collaboration paper. Thus, the contribution of the work, which will be presented in the following and which is discussed in the other papers/manuscripts, is only a small part of the collaboration paper.

Preface

In this work, it is shown, how natural radioactivity and cosmogenic muons contribute to the background of the Electron Capture in ^{163}Ho (ECHO) experiment. In order to analyze signals, which are acquired with the ECHO detectors and caused by muons, an active muon veto was operated in parallel to a measurement. A pulse shape analysis was developed to recognize the muon-generated pulses and refined to study signals acquired with non- ^{163}Ho -loaded ECHO detector pixels.

The results of this work are published in [7] “Göggelmann, A. *et al.* Study of naturally occurring radionuclides in the ECHO set-up. *Eur. Phys. J. C* **82**, 139 (2022)” and [8] “Göggelmann, A. *et al.* Study of muon-induced background in MMC detector arrays for the ECHO experiment. *Eur. Phys. J. C* **81**, 363 (2021)”. This thesis refers to this two publications.

After a short introduction (Chapter 1), the results of Monte Carlo (MC) simulations presented in [7] and [8] are summarized in Chapter 3. Both works are sharing the simulation set-up shown in Section 3.1. The results of the MC simulation of muons passing the ECHO set-up, which are discussed in [8] are summarized in Section 3.2. This section is followed by Section 3.3 including a summary of results of MC simulations of natural radioactivity in the ECHO set-up, which are discussed in [7].

The analysis of background signals [7] and muon-generated signals [8] are discussed in Chapter 4. The pulse shape analysis method, which is introduced in [8] and discussed in more detail in the non-submitted manuscript “A pulse shape analysis for the ECHO experiment”, is introduced in Section 4.1. After the introduction of the pulse shape analysis method, the analysis of muon-induced signals (Section 4.2), which is presented in [8], is summarized. The last section of this chapter (Section 4.3) includes the summary of the analysis of signals acquired with non- ^{163}Ho -loaded detector pixels discussed in [7].

“C. Velte *et al.* High-resolution and low-background ^{163}Ho spectrum: interpretation of the resonance tail. *Eur. Phys. J. C* **79**, 1026 (2019)” is a collaboration paper, which discusses the data acquisition and data analysis in a proof of concept experiment spectrum. This experiment was performed in the underground laboratory in Modane (Laboratoire Souterrain de Modane LSM), which resulted to a reduction of the muon flux in respect to sea level (4800 m water equivalent). Four detector pixels were operated for four days. Due to the short exposure time of 16 pixel-days and the reduced muon flux, the discussion of background was not very important. The only two events, present in the spectrum, were in a region in which different background sources could be responsible. The possibility to develop a precise background spectrum, in order to be able to identify the most probably background source and following, being able to develop methods to reduce background contributions, is of utmost importance for the ECHo experiment.

Chapter 1

Introduction

Since ancient times, mankind was observing the universe and aiming to understand the origin and evolution of such a complex system. Despite of ancient philosophers like Aristotle (384 - 322 B.C.) and Democritus (ca. 460 - 370 B.C.), who tried to explain the behavior of our solar system and the structure of matter, it took approximately further 2000 years until humanity began to give a description of the astronomical objects and their dynamics, which were based on solid concepts, like the heliocentrism related mainly to the figure of Nicolaus Copernicus (1473 - 1543). With the discovery of electrons by Sir Joseph John Thomson in 1904, the story of the discovery of elementary particles began, which finally led to the Standard Model of particle physics. One of the last open questions of the (extended) Standard Model is the determination of the mass scale of neutrinos, the particles postulated by Wolfgang Pauli in 1930 [9] and discovered in the Cowan-Reines neutrino experiment in 1956 [10]. With the Homestake experiment [11], the solar neutrino problem has been drawn to attention and was solved by the SNO experiment [12] and Super-Kamiokande experiment [13], in which the neutrino oscillation was discovered, leading to the fact, that neutrinos have a non-vanishing mass. Neutrino oscillation experiments provide quite precise values for the difference in neutrino mass square [14,15], but no information on the absolute mass scale. Presently, only upper limits on quantities related to neutrino masses are available [16–18].

1.1 Neutrino Masses

The following section based on [19], which is only one of many review articles of neutrino physics.

By the thermonuclear reactions in the sun, many electron neutrinos are generated as described in the Standard Solar Model (SSM). These neutrinos are detected in different experiments [11,20–27]. However, with the pioneer Home-

stake experiment, the solar neutrino problem arrived, because the detected electron neutrino flux was only about a third of the expected flux motivated by the SSM [28]. The same deficit in the detected solar electron neutrinos was also occurring in other experiments, which are characterized by different detection methods and therefore, characterized also by different energy thresholds. The solar neutrino problem was finally solved with the discovery of the neutrino oscillation by the combined work of the SNO experiment [12], which was demonstrating that the flux of neutrinos from the sun was as expected from the SSM, if all neutrino flavors were measured, and of the Super-Kamiokande experiments [13], which measured muon neutrinos generated in the atmosphere as a function of the incoming direction. The neutrino oscillation, meaning the transitions between neutrino flavors, can only occur, if at least two of the three¹ mass eigenvalues m_1 , m_2 and m_3 of neutrinos are larger than zero, since the transition probability between two neutrino flavor states depends on the non-zeros mass differences of the mass eigenvalues. The mass difference $\Delta m_{21}^2 = m_2^2 - m_1^2$, determined by the detection of solar neutrinos and described by the Mikheyev-Smirnov-Wolfenstein effect, and determined also by analyzing the $\bar{\nu}_e$ survival probability in the KamLAND experiment [26], is about $\Delta m_{21}^2 = 7.55^{+0.20}_{-0.16} \cdot 10^{-5} \text{ eV}$ [15]. The mass difference $\Delta m_{32}^2 = m_3^2 - m_2^2$ is about $\Delta m_{32}^2 = (2.42 \pm 0.03) \cdot 10^{-3} \text{ eV}$ [15], which is determined by investigating atmospheric neutrinos [29–31], accelerator neutrinos [32–35] and reactor neutrinos [36–38].

1.1.1 Neutrino Cosmology

A non vanishing total neutrino mass has influence on several cosmological parameters. It changes the Cosmic Microwave Background (CMB) lensing [17] and the structure formation in the universe [39, 40]. In the analysis of the DES collaboration, the upper limit for the sum of all neutrino masses is determined by fixing the effective number of neutrino species to $N_{\text{eff}} = 3.044$, which is predicted by the standard cosmology model [41, 42] and lies within the boundaries of several experimental results [17, 43, 44]. Resulting, the upper limit for the sum of all neutrino masses is determined to $\sum m_i < 0.13 \text{ eV}$ at 95 % C.L. [45].

1.1.2 Direct neutrino mass measurement

The neutrino was first postulated by Pauli to protect the energy-momentum conservation in the β -decay. The β -decay of tritium, ${}^3\text{H} \rightarrow {}^3\text{He} + e^- + \bar{\nu}_e$, was

¹Assuming non-existing sterile neutrinos.

used in the Mainz [46] and Troitsk [47] experiments to determine the effective electron anti-neutrino mass with a model-independent kinematic method, leading to an upper limit for the effective electron anti-neutrino mass of $m_{\bar{\nu}_e}^{\text{eff}} < 2.2$ eV at 95 % C.L. The energy spectrum of the emitted electron depends directly on the neutrino masses m_i :

$$\frac{dN}{dE} \propto \sum_i R(E) \Theta(E_0 - E - m_i) |U_{ei}|^2 (E_0 - E) \sqrt{(E_0 - E)^2 - m_i^2}, \quad (1.1)$$

with the Heaviside function $\Theta(E_0 - E - m_i)$, the maximum available kinetic energy for the electron of $E_0 = Q - m_e \approx 18$ keV and the lepton mixing elements for the electron neutrino U_{ei} . $R(E)$ contains the Fermi function and the phase-space factor of the electron. The recent upper limits for the 90 % C.L. of the effective electron anti-neutrino mass $m_{\bar{\nu}_e}^{\text{eff}} = \sqrt{\sum |U_{ei}|^2 m_i^2}$ is received by the currently running KATRIN experiment [16] with $m_{\bar{\nu}_e}^{\text{eff}} < 0.8$ eV. Besides the KATRIN experiment, Project 8 [48] also investigates the decay of (atomic) tritium by cyclotron radiation.

A radioactive-decaying isotope with a smaller Q -value than for tritium is the electron capture (EC)-decaying ^{163}Ho : $^{163}\text{Ho} + e \rightarrow ^{163}\text{Dy}^* + \bar{\nu}_e$ with $Q_{\text{EC}} \approx 2.8$ keV. This decay is currently studied by the ECHo [49], HOLMES [50] and NuMECS experiments [51]. These experiments measure calorimetrically the energy released by the de-excitation of the ^{163}Dy atom. Note that these experiments are sensitive to the effective mass of the electron neutrino, which is different to the tritium experiments. The energy spectrum of the de-excitation of the excited ^{163}Dy atom is similar to Eq. (1.1) by replacing E_0 with Q_{EC} and $R(E)$ with Breit-Wigner resonances. The recent upper limit for the effective mass of the electron neutrino from the ECHo experiment is $m_{\nu_e}^{\text{eff}} < 150$ eV at 95 % C.L. [5].

1.2 The ECHo Experiment

In order to determine the effective mass of the electron neutrino, the Electron Capture $^{163}\text{Holmium}$ (ECHo) experiment [49] was designed. To achieve this, ^{163}Ho is implanted in the absorbers of the metallic magnetic calorimeter (MMC)-based detector pixels [52, 53]. The ^{163}Ho atoms decay via an EC process by emitting an electron neutrino and leaving the daughter atom in an excited state. The spectrum of emitted energy minus the energy of the neutrino is characterized by resonances with these excited states and the emission of X-rays and Auger-electrons [54, 55]. The blue curve in Figure 1.1 shows this energy spectrum. Due to the very small neutrino mass, only the region around

$Q_{\text{EC}} = (2833 \pm 30_{\text{stat}} \pm 15_{\text{sys}}) \text{ eV}$, which is the maximum energy available for the EC, is mostly affected by a non-vanishing neutrino mass (compare to the insert of Figure 1.1). Q_{EC} was measured using the double Penning Trap SHIP-TRAP [56] and is given by the mass difference between the ^{163}Ho atom and its daughter atom ^{163}Dy .

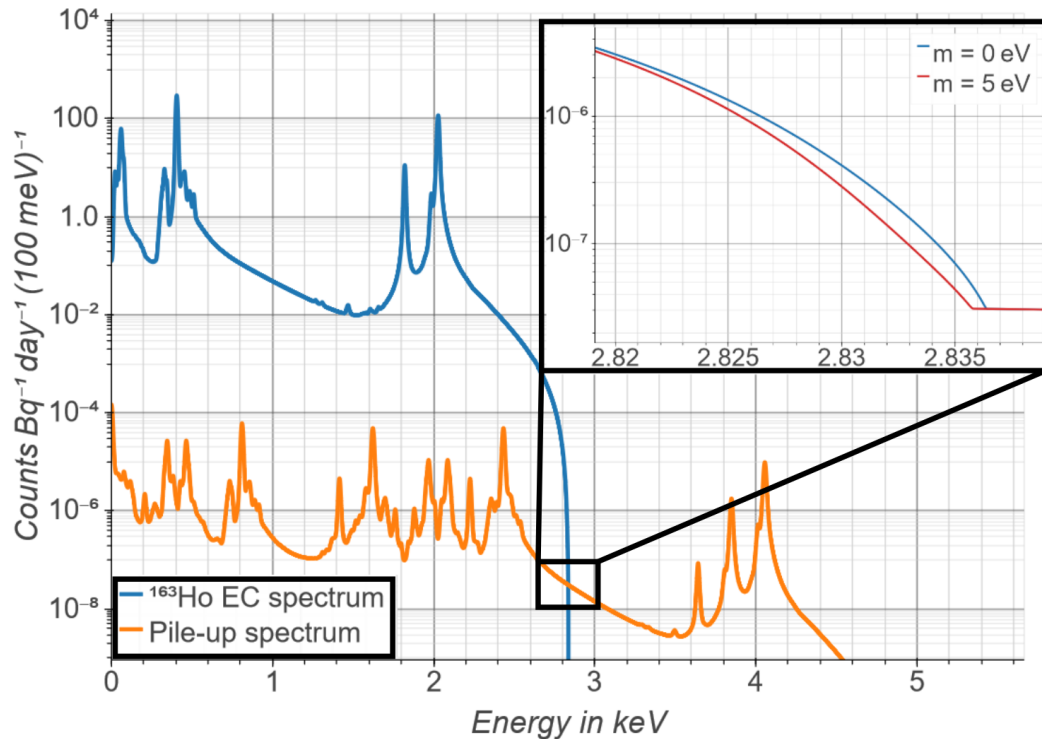


Figure 1.1: Expected ^{163}Ho EC spectrum [54] calculated by using $Q_{\text{EC}} = 2833 \text{ eV}$ (blue curve). The related unresolved pile-up spectrum of equal and opposite polarity signals and a pile-up fraction of 10^{-6} is shown in orange. An energy resolution of $\text{FWHM} = 10 \text{ eV}$ is used. **Insert:** The effect of massive neutrinos on the summed spectrum (EC spectrum plus pile-up) is shown. Picture taken from [7].

1.2.1 Metallic Magnetic Calorimeters

The MMCs consist of a paramagnetic sensor, which sits in a static magnetic field and is connected to a gold absorber [57]. The sensor and absorber are characterized by their thermodynamical properties, in particular their heat capacity, which is important to determine the increase of temperature due to the deposition of energy, C_s , which represents the heat capacity due to the spin system of the sensor, and C_e representing the heat capacity due to the electron

system of the detector. By the conduction electrons of the absorber, the energy deposited in the absorber is very quickly distributed over the whole detector. Then, the energy is transferred from the electron system to the spin system in the sensor, which changes the sensor's magnetization [52, 58]. This change of magnetization is then converted to a change of voltage using superconducting quantum interference device (SQUID)s, especially dc-SQUIDs. Further, the absorber is connected to a thermal bath through a weak link with a thermal conductance G_{eb} , so that the base temperature of the detector can be fixed.

The time profile of the voltage signal $U(t)$ of a MMC is proportional to the change of temperature of the MMC, which itself is proportional to the deposited energy E and can be described by the sum of two exponential functions [52]:

$$U(t) \propto E \cdot (e^{-t/\tau_d} - e^{-t/\tau_r}), \quad (1.2)$$

with the rise time τ_r and the decay time τ_d . Both time constants, τ_r and τ_d , depend on the thermal conductivities and heat capacities of the systems [52]. The decay time is in the order of ms and approximately given by the thermal conductance and heat capacity

$$\tau_d = \frac{C_e + C_s}{G_{\text{eb}}}. \quad (1.3)$$

The rise time depends on the electron spin interaction, which is defined through the Korringa constant κ and by the fraction of C_s to the total heat capacity

$$\tau_r = \kappa \cdot \left(1 - \frac{C_s}{C_e + C_s}\right). \quad (1.4)$$

The rise time defines approximately the time resolution of the detector of about 500 ns for ECHO-1k. However, due to the readout bandwidth limitation, the rise time of the signal can be even larger [57].

These relations of the time constants only apply for particles stopped in the absorber of the MMCs. If a particle deposits energy directly in the sensor, a fraction of the deposited energy could be transferred to the spin system in shorter times. Or, if energy is deposited in the substrate next to sensor and transported to the sensor, the effective total heat capacity of this system is higher, which results in a larger rise time.

1.2.2 Experiment Set-Up

Each MMC consists of two detector pixels with dimensions of about $180 \mu\text{m} \times 180 \mu\text{m} \times 10 \mu\text{m}$ (see Section 3.1 for more details). The two detector pixels of

each MMC can be readout by the same SQUID, because of the so-called double-meander geometry of the pick-up coils. A pair of two pixels connected to the same SQUID is called channel, which can accordingly raise signals with positive and negative polarity. The thermodynamical properties of two pixels of the same channel are nearly identical. In the first stage of the ECHo experiment, called ECHo-1k, 72 detector pixels are used, from which 64 pixels (32 channels) can be readout simultaneously. Two channels (four pixels) can be used to measure the temperature of the chip, seven pixels of seven different channels are not loaded with ^{163}Ho and can be used to measure the background. Resulting, eleven pixels are not implanted. The other 61 pixels are loaded with ^{163}Ho . For the ECHo-1k chip [57], the pixels are arranged in an array of four rows and 16 columns. The ^{163}Ho activity per pixel is about 1 Bq, leading to a very small expected count rate of about $8 \cdot 10^{-5}$ counts day $^{-1}$ pixel $^{-1}$ in the region of interest (ROI), the last 10 eV below the Q_{EC} -value. Accordingly, the background level in the order of 10^{-6} counts day $^{-1}$ pixel $^{-1}$ has to be controlled. In the future stage of the ECHo experiment, ECHo-100k, the ^{163}Ho activity per pixel will be increased to about 10 Bq leading to a signal count rate as high as ten times the count rate in ECHo-1k.

1.3 Background Sources

1.3.1 Unresolved pile-up

When two ^{163}Ho atoms decay in the same pixel or in two pixels of the same channel within a time interval less than τ_r , the two events can not be distinguished and the total deposited energy will be connected to a single event. In first approximation, the count rate of these pile-up events is given by the ^{163}Ho activity A per pixel and the time resolution τ_r and is $r_{\text{pu}} = 2 \cdot A^2 \cdot \tau_r$, if two pixels of the same channel are loaded with the same amount of ^{163}Ho . A pile-up spectrum for a pile-up fraction of $f_{\text{pu}} = 2 \cdot A \cdot \tau_r = 10^{-6}$ is shown as the orange line in Figure 1.1. The pile-up rate in the last 10 eV below Q_{EC} is expected to be about $3 \cdot 10^{-6}$ counts day $^{-1}$ pixel $^{-1}$, with an ^{163}Ho activity per pixel of 1 Bq and a time resolution of $\tau_r = 500$ ns.

The resolvable time difference between two events depends on the pulse shape analysis methods. If fitting a template pulse to each pulse for example, the corresponding χ^2 -value depends on the amplitude of the second pulse. Thus, the pile-up spectrum received after the pulse shape analysis could be different compared to the shown spectra [6].

1.3.2 Electromagnetic noise

Electromagnetic radiation like the “Global system for mobile communication” can couple to the readout chain of the detectors and can generate background signals. The shape of this kind of signals is unique and can easily recognized [6, 59]. Based on the difference between trigger time stamps of events, these events can also be rejected with an efficiency of almost 100 % [6].

1.3.3 Co-implanted isotopes

Radioisotopes like $^{166\text{m}}\text{Ho}$ [60], ^{170}Tm or ^{171}Tm [61] are produced in the ^{163}Ho -production process. If these isotopes are implanted in the detector pixels, those nuclides would generate an addition background. However, the concentration of those isotopes in the ^{163}Ho samples are minimized in the ECHo experiment in a two-step separation: First, a chemical separation is used to ensure that no elements different to holmium are left after the production process [61] and second, the $^{166\text{m}}\text{Ho}/^{163}\text{Ho}$ fraction is reduced by mass separation at the RISIKO facility [62]. With this, a total $^{166\text{m}}\text{Ho}/^{163}\text{Ho}$ ratio below $5 \cdot 10^{-10}$ is achieved in the MMCs, which is far below the critical level of 10^{-4} resulting from Monte-Carlo simulation of $^{166\text{m}}\text{Ho}$ [63, 64].

1.3.4 Natural occurring radionuclides

Due to the very low sensitive energy range of the ECHo experiment of less than 3 keV, mainly low energy radiation generated in the near vicinity of the active volume of the detector should contribute to the background. On the one hand, low energy radiation is mainly produced by β -decaying or EC-decaying nuclides, while on the other hand, low energy Auger electrons and X-rays can also be emitted after an α -decay. The most frequent naturally occurring radionuclides in materials are nuclides like ^{40}K , ^{238}U , ^{232}Th and daughter nuclides of their decay chains.

^{238}U and ^{232}Th can be found with an abundance of about 3 mg kg^{-1} and 10 mg kg^{-1} in the earth’s crust respectively [65] and accordingly, they and theirs daughters also occur in concrete and in metals. Resulting, typical concentration in pure metals are in the order of $(0.1 - 1) \text{ mBq kg}^{-1}$ [66–68] and concentrations about $(1 - 2) \text{ Bq kg}^{-1}$ in non-pure metals and alloys [69]. Gaseous radionuclides, such as the ^{238}U -daughter ^{222}Rn can be accumulated in indoor air with concentrations of the order of 10 Bq m^{-3} [70] and can further be accumulated on surfaces. Accordingly, ^{222}Rn and thus, ^{210}Pb atoms can be implanted in the detector materials. Concentrations of ^{210}Pb and ^{210}Po of the order of $10^{-4} \text{ mBq cm}^{-2}$ are typically for metal surfaces [71]. ^{40}K is present

in natural potassium with an abundance of 0.0117% [72]. It occurs in organic materials like the human body and plastics. Crude oil and coal are often basic materials for plastics, binders (plastic dispersions) and solvent and are known to have levels of radioactive concentrations of about tens to hundreds of Bq kg^{-1} [73–75].

1.3.5 Cosmogenic muons

Muons generated in the upper atmosphere by cosmogenic radiation can interact with the material of the set-up and can either deposit energy in the detector pixels or can generate secondary radiation by interacting with the material in the surrounding of the detector, which can also deposit energy in the active volume of the detector. At sea level, the muon flux is about $180 \text{ muons s}^{-1} \text{ m}^{-2}$ [19], leading to a muon flux of about $0.5 \text{ muons pixel}^{-1} \text{ day}^{-1}$ or $780 \text{ muons day}^{-1}$ for the ECHO-1k chip.

Not all muons, which interact with the ECHO-1k chip, generate events with energies less than 4 keV. The energy deposition of muons passing the detector pixels depends on the energy and on the angular distribution of the muons [76, 77]. While the mean energy loss due to ionization does not change much for different muon energies, the path length of the muons traveling through the pixels strongly depends on the arriving angle of the muons and on the thickness of the pixels. A calculation of the deposited energy of muons passing through the detector pixels is shown in Figure 1.2 for different absorber thicknesses and by considering the straggling of the energy loss by ionization [78]. According to these calculations, only short muon path lengths in the gold absorbers (meaning thin absorbers) would lead to energy depositions of less than 3 keV. However, energy loss due to resonances with the atomic shell levels of gold, which are less than 4 keV for the M, N and O shells, are not included here, but should also occur in the experiment. This is why the probability, that a muon deposits less than 4 keV, is underestimated here. It was shown that the energy loss straggling distribution in thin silicon detectors gets smeared for lower energies, if resonances with the atomic shell levels are included [79]. The same effect can be assumed for thin gold detectors.

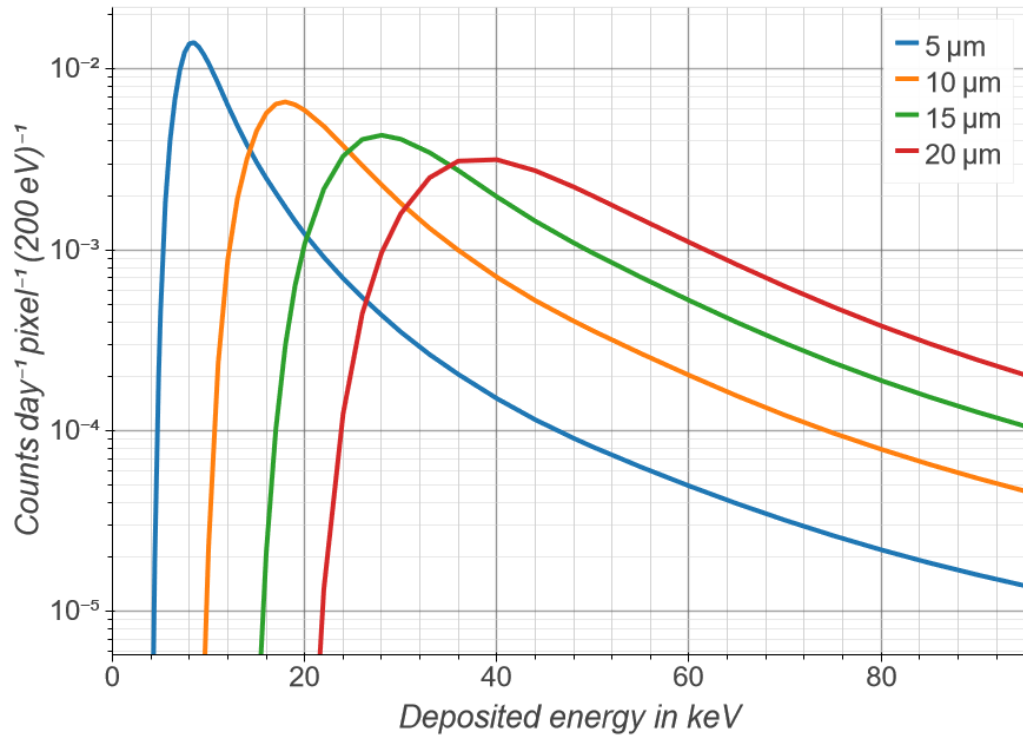


Figure 1.2: Distribution of the energy deposited by muons passing gold absorbers with areas of $180 \mu\text{m} \times 180 \mu\text{m}$ and different thicknesses. Calculated with the muon momentum spectrum given in [76], with the angular distribution given in [77] and with the energy loss described in [78,80]. Figure taken from [8].

Chapter 2

Objective

In order to reach sub-eV sensitivity on the effective electron neutrino mass in the ECHo experiment, the identification and reduction of background are of utmost importance. It is aimed to reduce the background contributions below that of the unresolved pile-up of the order of 10^{-6} counts day⁻¹ pixel⁻¹ in the ROI.

A pulse shape analysis is developed to separate events due to particles stopped in the detector pixels, like the decay of enclosed ¹⁶³Ho in the pixels, from other pulse families caused by energy deposited in other parts of the detector.

Muonic background is studied by analyzing events coincidental to an active muon veto installed around the cryostat used for the operation of the detectors. With pulse shape analysis methods, muon-generated events can be used as a sample of events related to energy deposition in the substrate of the ECHo-1k chip. Monte Carlo simulations of muons interacting with the detector materials are performed to give predictions of a muon related background.

The impact to the background spectra of natural radioactive isotopes, close to the active detector volume, are studied using Monte Carlo simulations including information of material screening measurements. The results of the simulations are compared to background spectra acquired in detector pixels with and without implanted ¹⁶³Ho.

Chapter 3

Monte Carlo Simulations

The performed Monte Carlo simulations in this work [7, 8] are based on version 10.06.p03 of the GEANT4 toolkit [81]. Due to the low energy range of the ECHo experiment of less than 4 keV, low energy particles have to be generated and propagated in the simulations. In processes with infrared divergence (e.g. production of bremsstrahlung and δ -rays¹), infinitely many particles with energies near 0 keV are generated, if no particle production energy threshold is set. The predefined particle production energy thresholds are configured for two reasons: On the one hand to decrease the computation time as much as possible and on the other hand, to study accurately the effect of low energy particles generated in the surrounding of the detector pixels. If a particle produced by a process with infrared divergence has a kinetic energy smaller than the energy threshold, the particle will not be generated in the simulation and its energy will be deposited locally. Particles generated by other processes like particles generated by radioactive decays or atomic de-excitation are not affected by this cut.

3.1 Set-Up

Figure 3.1 shows the simplified set-up of the ECHo-1k experiment used in the simulations, which is described in [7] and [8]. The ECHo-1k chip is made of silicon with dimensions of 10 mm x 5 mm and a thickness of 350 μm [57]. On top of the chip, 36 MMC pairs are located in an array of four lines, resulting in 72 pixels. The pixels consist of gold absorbers of dimensions 180 μm x 180 μm x 10 μm directly above of **Ag:Er** sensors of dimensions 168 μm x 168 μm x 1.35 μm [1, 57]. Thin 200 nm layers of silver with areas of about 150 μm x 150 μm are in the middle of the absorbers. The array of 4 x 18 pixels can be seen in the insert of Figure 3.1.

¹Free electrons produced by ionization.

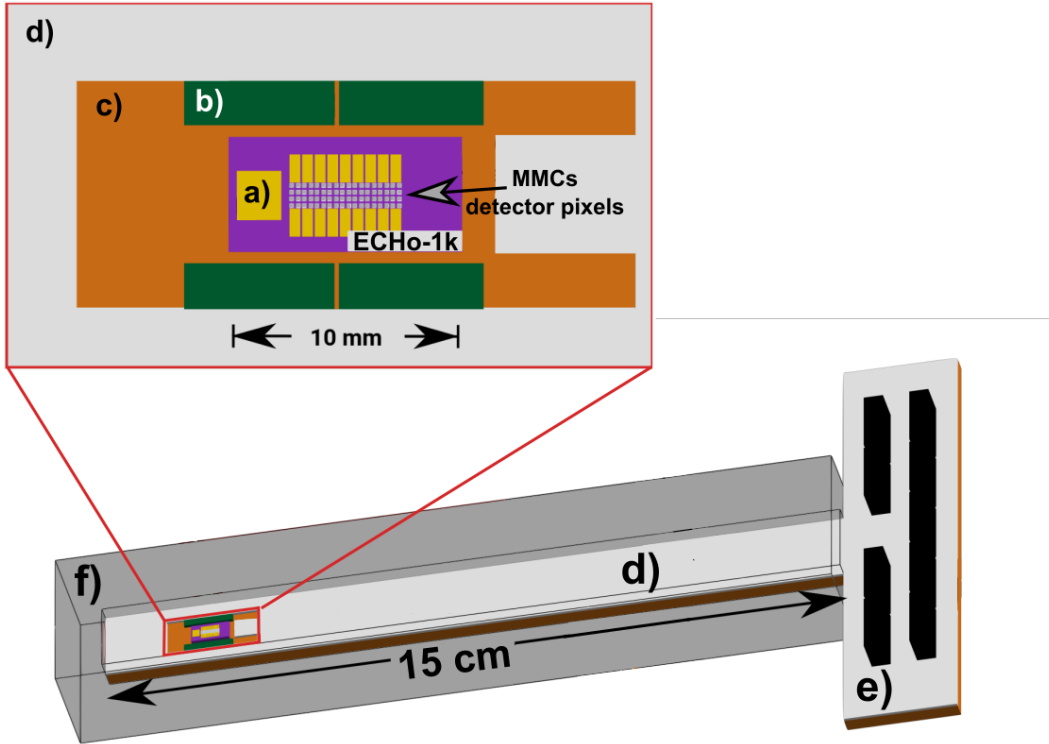


Figure 3.1: Simplified design of the ECHO-1k experiment setup used in the simulation. **Insert:** The ECHO-1k chip and the near surrounding. 72 MMCs and large thermalization structures (a) are located on top of the purple colored silicon ECHO-1k chip. The ECHO-1k chip and four dc-SQUID chips (b) are next to the ECHO-1k chip. All five silicon based chips are directly placed on the copper holder (c). The copper holder is completely covered by a circuit board (d), except the region next to the ECHO-1k chip. Nine connectors (e) are placed at a distance of about 15 cm from the ECHO-1k chip. An aluminum box (f) surrounds the set-up. Picture taken from [7].

Larger gold structures are positioned next to the pixels (Figure 3.1 (a)). The four silicon dc-SQUID chips with dimensions of 6 mm x 2.5 mm and thickness of 350 μm are close to the ECHO-1k chip (Figure 3.1 (b)). The copper support has a thickness of 0.7 cm (called copper holder, Figure 3.1 (c)) and is covered by the circuit board (Figure 3.1 (d)) with a thickness of 0.7 mm. In the simulation, the circuit board is made of a bisphenol-based epoxy resin. The rectangular aluminum tube of 2.5 cm (width) x 0.9 cm (height) and a length of 15 cm surrounds the set-up (Figure 3.1 (f)). The wall thickness of the aluminum tube is 3 mm for the bottom and top side and 10.3 mm for the other sides. At a distance of about 15 cm to the ECHO-1k chip, nine carbon-based connectors with a density of 1 g mol^{-1} (in the simulation) are placed (Figure 3.1 (e)).

The shorter the distance to the detector pixels, the more the energy threshold of particle production is being reduced. The energy threshold is equivalent to a minimum distance the particles have to pass before getting fully stopped. These minimum ranges are shown in Table 3.1 for different volumes. The larger volumes like the copper holder, aluminum shielding and the substrate of the ECHO-1k chip, contain sub-volumes. The sub-volumes with their dimensions and cut values are shown in Figure 3.2, which shows the profile of the set-up around the ECHO-1k chip.

Volume	Min range
MMCs	100 nm
Thermal baths	100 nm
(*)Substrate	1.0 μm
SQUID chips	1.0 μm
Circuit board	10 μm
Plugs	1.0 mm
(*)Copper holder	1.0 mm
(*)Shielding	1.0 mm

Table 3.1: The minimum ranges that the particles have to pass within different volumes. If a particle has not enough energy to travel as far as the minimum range, the particle will not be created in the simulation and its energy will be deposited locally. Larger volumes, marked with (*), contains sub volumes with smaller minimum range cuts (see Figure 3.2). Table taken from [8].

3.2 Muons

In the following section, the simulation of muons, described in [8], is summarized. Muons are simulated in a way that they have to travel through the ECHO-1k chip. The energy and the angular distribution of the muons follows [76]. The set-up is spatially placed, such that the pixels are parallel to the ground. Mostly, energy is deposited directly in the detector pixels by muons. The major part of secondary radiation depositing energy is due to δ -rays generated in the surrounding. The distribution of the deposited energies of the different contributing radiation is shown in Figure 3.3. The simulated spectrum above 10 keV (Figure 3.3a) is in good agreement with the Landau distribution [78], which describes the energy loss of minimal ionization particles, and for an absorber thickness of 10 μm (compare to Figure 1.2).

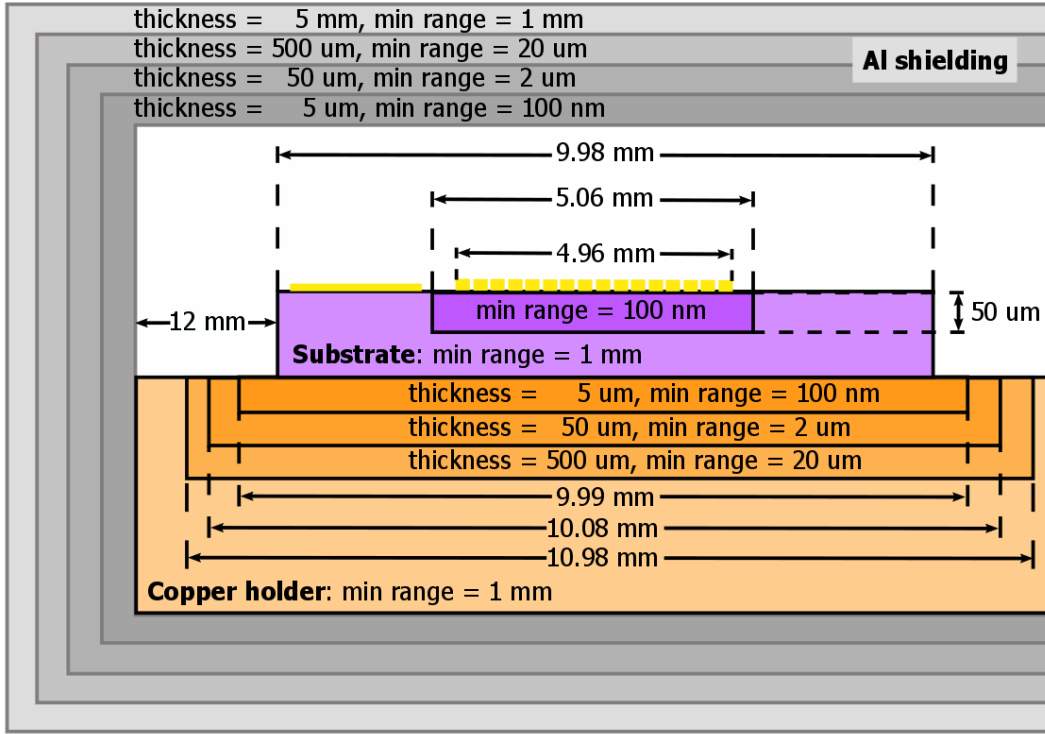


Figure 3.2: Scheme of the ECHO-1k chip and its surrounding (not to scale). The minimum ranges particles have to pass before getting fully stopped are shown for different sub volumes of the larger volumes. The dimensions of these sub volumes are shown, too. Picture taken from [8].

However, these energies corresponds to pulses with amplitudes higher than the acquisition window and therefore, are not recorded (the maximum energies, which can be measured corresponds to 5 keV to 6 keV). For smaller energies, the spectrum differs, as expected from resonances with the atomic shell levels (Figure 3.3b).

From the simulation, a count rate of approximately $(2.2 \pm 0.1) \cdot 10^{-5}$ counts day^{-1} pixel^{-1} is expected in the last 10 eV below Q_{EC} due to muon induced events. In the energy region of 0 keV to 4 keV, less than 10^{-2} counts day^{-1} pixel^{-1} are expected. For these calculations, a constant muon flux of $180 \text{ muons s}^{-1} \text{ m}^{-2}$ is assumed. However, the muon flux is not constant over time and location. The flux can vary in orders of 10% [82]. To take this into account, the event rate is also given for every muon passing the detector chip, which leads to an expectation of about $(2.1 \pm 0.1) \cdot 10^{-6}$ counts in the ROI or less than 10^{-2} counts in the first 4 keV. Most of these events should, however, be identified by the pulse shape analysis, since muons and muon-generated secondary radiation are mostly not stopped in the absorbers of the pixels and

deposit energy in the substrate as well. Considering only events caused by stopped particles, which can not be recognized with pulse shape analysis, about $(5 \pm 2) \cdot 10^{-7}$ counts day⁻¹ pixel⁻¹ or $(5 \pm 2) \cdot 10^{-8}$ counts muon⁻¹ are expected in the ROI. It has to be noted, that, with a coincidence window of 1 ms, none of the pixel events due to particles stopped in the absorbers are coincident to other pixels events.

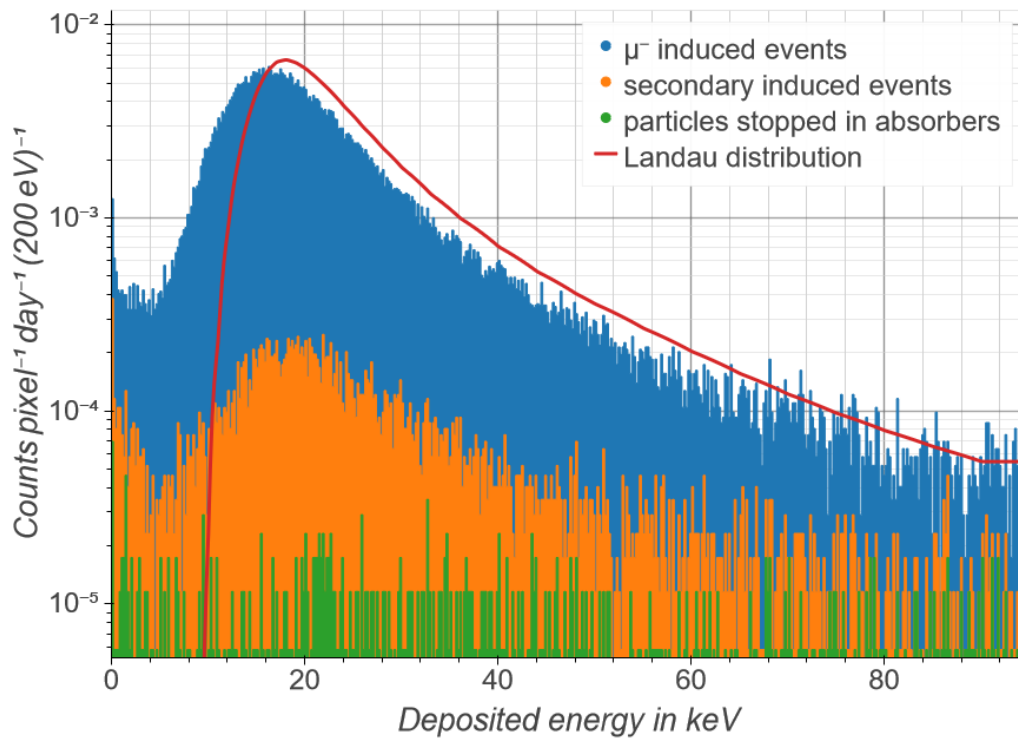
The expected count rates of events caused by muons are about one order of magnitude smaller than the unresolved pile-up rate with about $3 \cdot 10^{-6}$ counts day⁻¹ pixel⁻¹. The muonic background should be even smaller than the unresolved pile-up, if the muon flux is as high as two times 180 muons s⁻¹ m⁻², and thus, can be neglected.

Muons and secondary radiation can also deposit energy in the substrate next to the detector pixels. The local substrate heating can furthermore cause signals in the pixels. Such events are not included in the simulation, but could coincidentally occur with any other muon-generated events described above and can also be recognized by operating a muon veto in parallel to the detector.

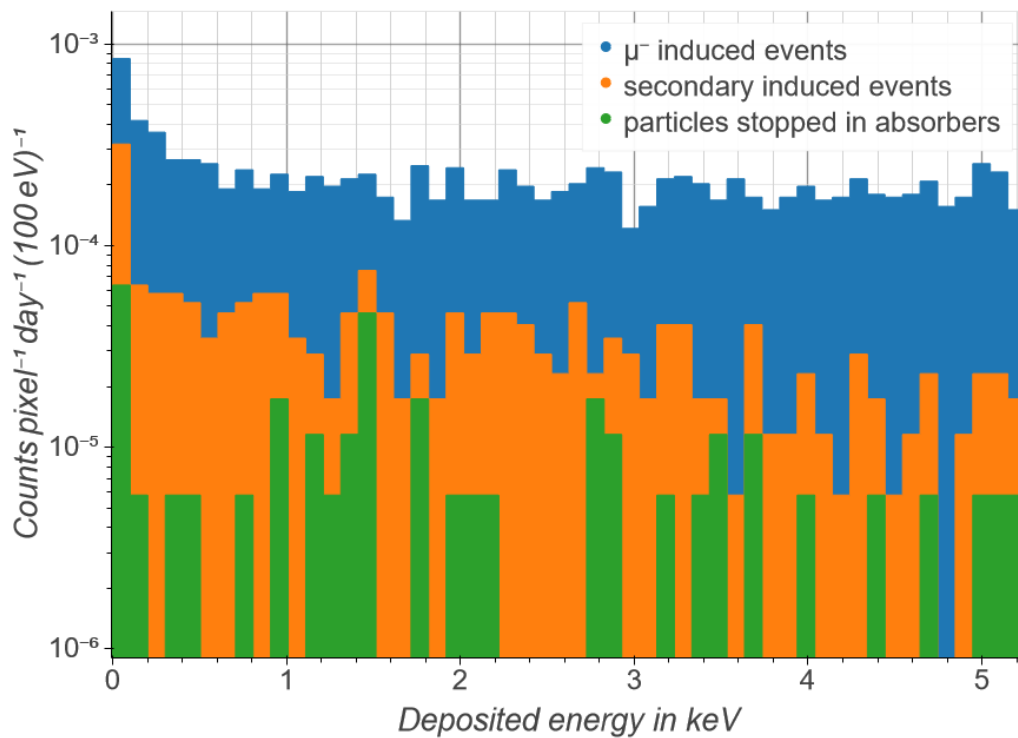
3.3 Natural Radionuclides

Radionuclides are simulated in [7] and discussed in the following. The simulations of radionuclides in the detector materials are divided into two sets: The simulation of bulk- and surface-distributed radionuclides. Bulk-distributed nuclides are uniformly distributed in the volume materials and uniformly distributed on the volume surfaces, if they are surface-distributed. The full decay chains of ²³⁸U, ²³²Th and ⁴⁰K are simulated, while being placed in different parts of the ECHO-1k set-up. Upper limits of tolerable concentrations are obtained by fitting an exponential distribution to the spectra of deposited energies and scaled, such that the count rate in the ROI caused by the radionuclides is equal to the expected rate of unresolved pile-up of about 10^{-6} counts day⁻¹ pixel⁻¹.

The upper limits of tolerable concentrations are much larger compared to the results of screening measurements, except for the circuit board. By assuming that ⁴⁰K is only surface-distributed, a total count rate of $(6 \pm 1) \cdot 10^{-6}$ counts day⁻¹ pixel⁻¹ is expected in the ROI, dominated by naturally occurring radionuclides in the circuit board (about 87%). This count rate is in the same order as the unresolved pile-up. The expected background spectrum caused by radionuclides in the detector materials is shown in Figure 3.4. In future, the circuit board will be made of polyimide based materials (Kapton), which have lower levels of radioactivity.



(a)



(b)

Figure 3.3: **a)** Simulated spectrum of the deposited energies in the detector pixels caused by muons (blue histogram) and secondary radiation, mostly δ -rays (orange histogram). Above 10 keV, the total energy distribution follows the Landau distribution for muons passing detectors with thicknesses of $10 \mu\text{m}$ (compare to Figure 1.2). **b)** The energy spectrum in the sensitive region of the ECHO experiment is nearly flat. Pictures taken from [8].

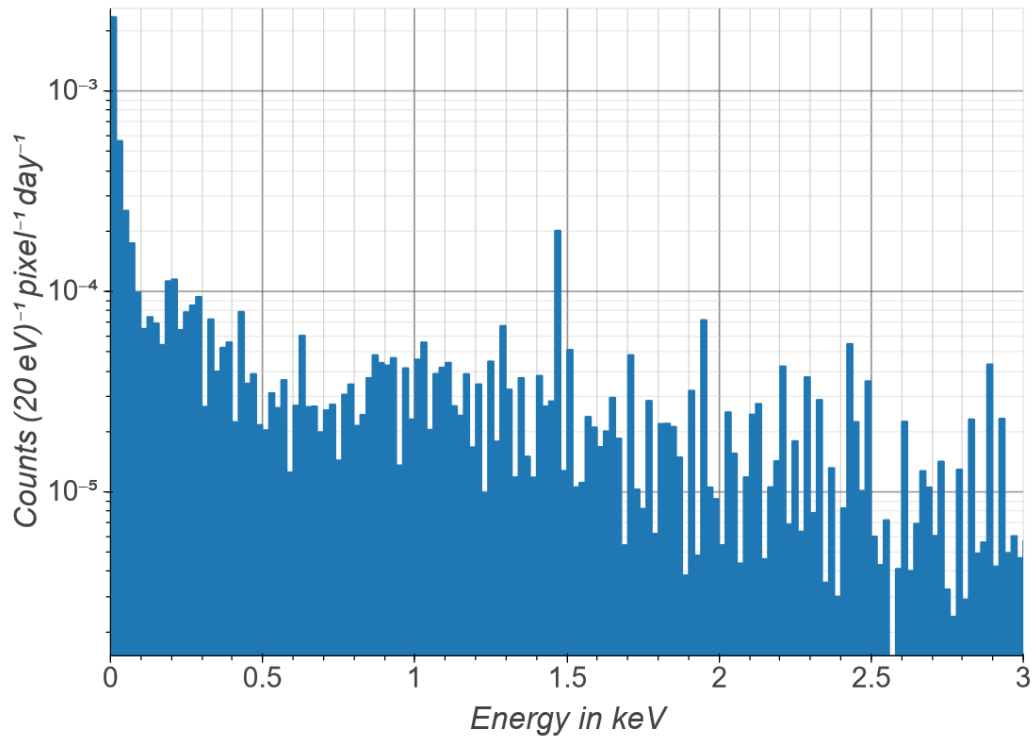


Figure 3.4: Simulated expected spectrum of deposited energies caused by natural occurring radionuclides in materials next to the detector arrays. The only visible structure is caused by 1.486 keV aluminum X-rays. Picture taken from [7].

For the first stage of the ECHo experiment, the background level of the order of 10^{-6} count day $^{-1}$ pixel $^{-1}$ is within the sufficient range, because a count rate of about 10^{-5} counts day $^{-1}$ pixel $^{-1}$ in the energy range of $Q_{EC} \pm 100$ eV is expected for concentrations as high as discussed. For an exposure of five months up to one year and 64 pixels, only a number of background events in the order of one is expected.

Chapter 4

Measurements

Two independent measurements were performed to study muon induced events [8] as well as background events [7].

Data set (1) A measurement including two channels with in total four ^{163}Ho -loaded pixels was performed by additionally operating an active plastic scintillator-based active muon veto. The measurement time was about 16 days, leading to an exposure of 64 pixel-days [8].

Data set (2) Five asymmetric channels, consisting each of one ^{163}Ho -loaded pixel and one pixel without ^{163}Ho (called background pixels), were operated between Dec 2019 and May 2020. Resulting, an exposure of about 241 pixel-days of ^{163}Ho -loaded and background pixels are acquired [7].

4.1 Pulse Shape Analysis

In the following, the pulse shape analysis method is introduced. This analysis is applied to both data sets and discussed in [8] and more detailed in [59].

The signals correspond to time traces with a length of about 2 ms. These traces include two parts, the pre-trigger, which corresponds to the first quarter of a trace, and the actual triggered signals. In the following, only the second quarter of a signal will be considered as a pulse in order to shorten the pile-up window.

Template fitting

The template signal is obtained by averaging 1000 to 5000 signals with amplitudes corresponding to energies of the ^{163}Ho -MI energy range. This is done for each pixel and each measurement day. The template signal of a ^{163}Ho loaded pixel is also used as a template signal for the background pixel corresponding to the same channel. An exemplary template signal is shown as the blue solid

curve in Figure 4.1. The actual used part, the second quarter of the template signal, is shown as the solid orange line. In the following, only this part will be considered, when talking about the template pulse. The template pulse is fitted to each pulse using the χ^2 method of varying the amplitude of the template. From this, the reduced χ^2 (i.e. χ^2/dof^{-1}), which describes the similarity of the template pulse and each signal pulse, is obtained. In addition, the template's tail, the last quarter of the template pulse (the green dotted part), is also fitted to each pulse to recognize pile-up within the length of the template pulse ($\delta t \approx 500 \mu\text{s}$) and results in the amplitude of the best fit A_{Template} . This method is sensitive to the overall pulse shape, but mainly to the falling edge of the pulses.

Filtering

The first fraction of the template pulse (approx. $100 \mu\text{s}$) is used to build a new time trace, called filter (red dotted line in Figure 4.1). This short length is chosen to become insensitive to pile-up on the falling edge of the pulses. Each pulse is correlated with this filter (so called matched filtering). The amplitude of the response function A_{Filter} describes mainly the area below the pulse around the rising edge (red area). This method is sensitive to the overall pulse shape around the rising edge.

Differentiation

The pulses are smoothed by using a moving average filter. The derivative of the smoothed pulses is calculated and the maximum of the derivative $A_{\text{Derivative}}$ is determined (compare to the red curve in Figure 4.1). This method is sensitive to pile-up with short time differences and to other effects, which could change the slope and rise time of the pulses, like energy transfer from the substrate to the sensor.

Integrating

The area A_{Integral} under the pulses is calculated. This method is sensitive to pile-up with large time differences and to other effects which could change the mean decay time (compare to the orange area in Figure 4.1).

Each of the four methods has a different sensitivity to the pulse shape. In order to distinguish between signals caused by the ^{163}Ho EC decay in the absorbers or by particles absorbed in the absorbers and signals caused by other processes, the ratio of the pulse shape parameters are considered. These ratios are the same for all energies for events caused by similar processes, but different for different processes. Meaning, the ratios are similar for single energy

deposition in the absorber volume, but scatter to arbitrary values for more complex energy depositions in the detector. For pulses due to the ^{163}Ho EC decay or similar, these ratios are set to one. Also, the reduced χ^2 is about one for these type of pulses.

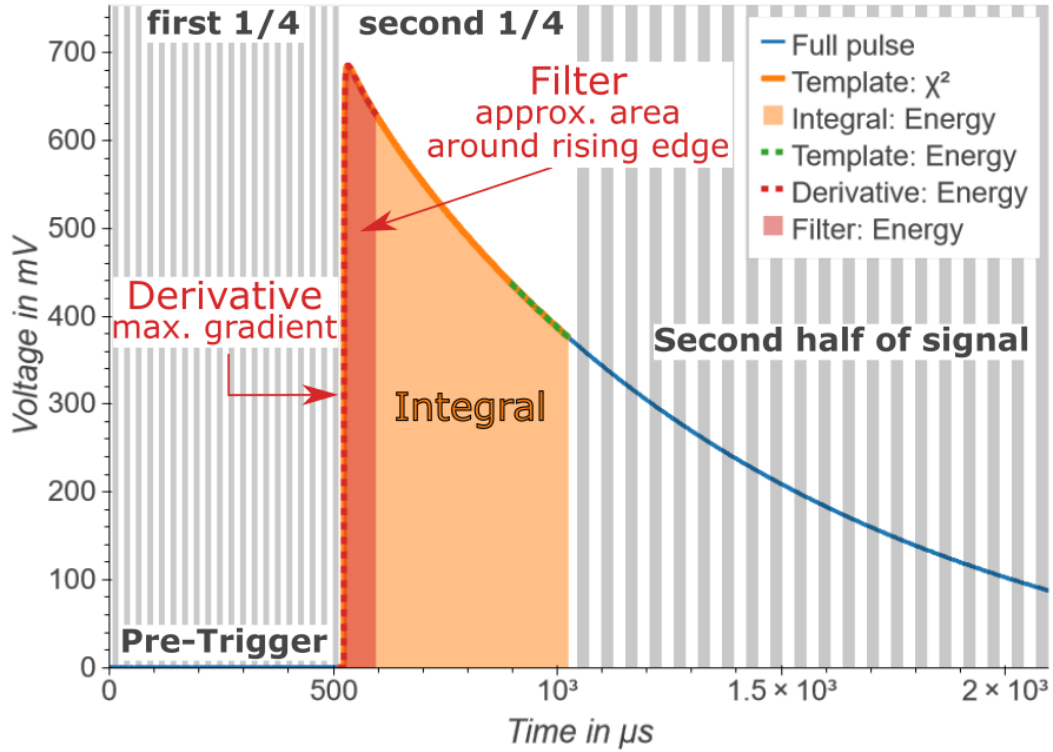


Figure 4.1: An exemplary template signal. The different colors show the different parts of the time trace used in the different analysis methods. A full template signal is shown as the blue solid line. The second quarter of the signal (orange line) shows the template pulse and is fitted to each pulse to obtain the reduced χ^2 . The tail of the template pulse (the last quarter, green dotted curve) is fitted to each pulse to obtain the amplitude of the fit. The first part of the template around the rising edge (red dotted curve) is cross-correlated with each pulse, resulting mainly in the area under the pulse around the rising edge (red area). The derivative of the smoothed pulses are calculated to obtain the maximum gradient. Last, the area under the pulses (orange area) is calculated.

Four methods are introduced, fitting of a **T**emplate, **F**iltering, **I**ntegrating and **D**ifferentiation, to describe the pulse shape. With these four energies, six ratios can be defined, $\frac{A_{\text{Derivative}}}{A_{\text{Template}}} = \text{DTR}$, $\frac{A_{\text{Derivative}}}{A_{\text{Filter}}} = \text{DFR}$, $\frac{A_{\text{Derivative}}}{A_{\text{Integral}}} = \text{DIR}$,

$\frac{A_{\text{Template}}}{A_{\text{Filter}}} = \text{TFR}$, $\frac{A_{\text{Template}}}{A_{\text{Integral}}} = \text{TIR}$ and $\frac{A_{\text{Filter}}}{A_{\text{Integral}}} = \text{FIR}$. From these, sets of three nonindependent parameters can be found. By calibration, these ratios are set to one for events caused by the decay of ^{163}Ho . Further, in the scatter plots of these ratios, ^{163}Ho induced events are located inside of ellipses located at $\text{ratio}_a \approx \text{ratio}_b \approx 1$ (compare to Figure 4.2).

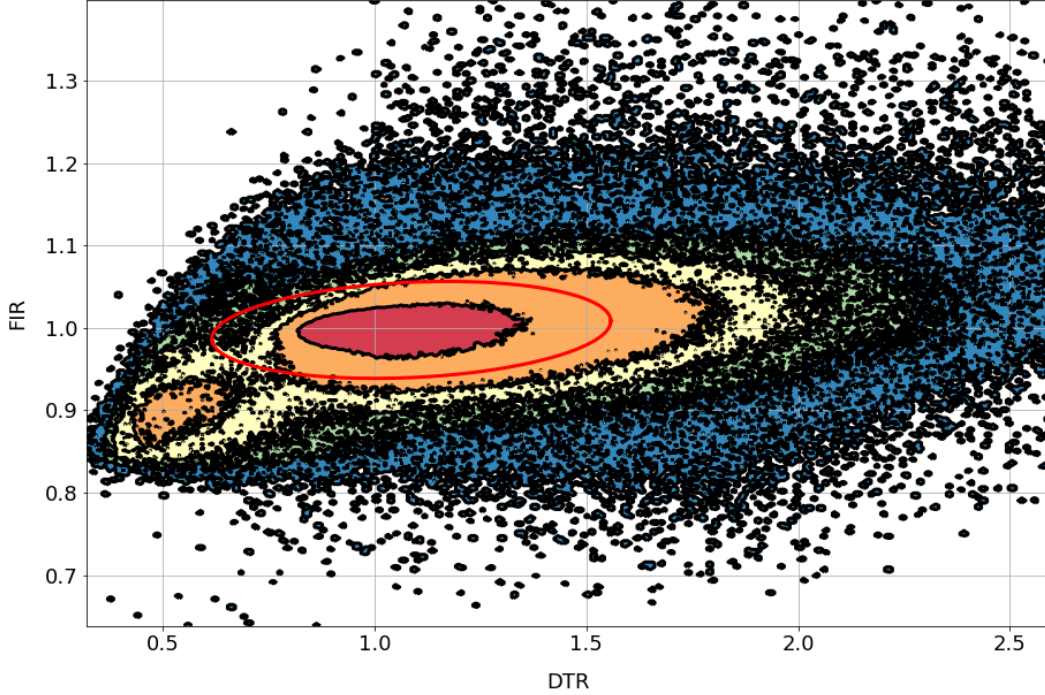


Figure 4.2: FIR parameter against DTR parameter of events of ^{163}Ho -loaded pixels. The contours of the density of events per bin are shown. The ^{163}Ho induced events are located in an ellipse around $\text{FIR} \approx \text{DTR} \approx 1$. The fitted ellipse is shown in red.

Five level contour plots are generated to obtain the ellipses. For this, event density plots in the ratio-ratio parameter spaces are generated. For instance as shown in Figure 4.2 for the FIR-DTR parameter space. The ratio between the major and minor axes, the rotation angle and position of each ellipse is determined by fitting an ellipse to the innermost (red colored) contour. The absolute lengths of the minor and major axes are determined by scaling the ellipses in a way, that the spectrum of χ^2 values of events inside the ellipses are well described by a χ^2 distribution. For this, the residuals obtained by fitting a χ^2 distribution to the χ^2 spectrum for different ellipse scales are calculated

(see Figure 4.3). Further, the residual distribution is fitted by a β -distribution

$$\beta(x, a, b) = \frac{\Gamma(a + b)x^{a-1}(1 - x)^{b-1}}{\Gamma(a)\Gamma(b)}, \quad (4.1)$$

with the gamma function $\Gamma()$. The minimum of the fitted β -distribution defines the ellipse scale, which means that the χ^2 spectrum of events inside an ellipse with this scale is best described by a χ^2 distribution.

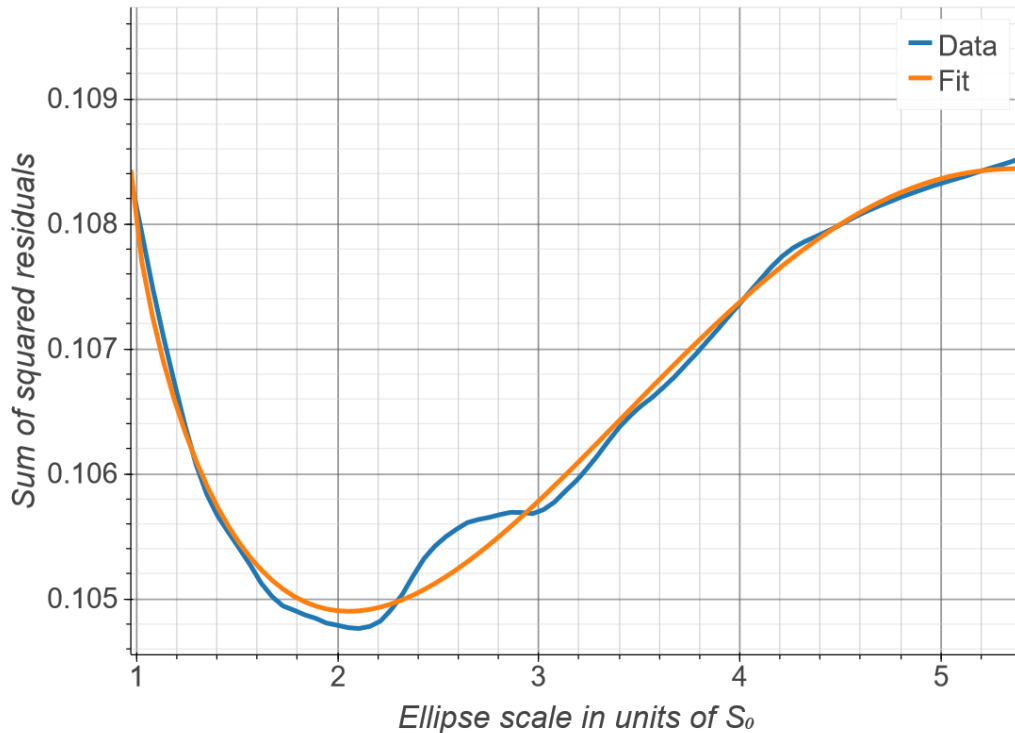


Figure 4.3: Sum of squared residuals for different ellipse scales. The residuals are determined by fitting a χ^2 distribution to the spectrum of χ^2 of events inside ellipses with different scales. S_0 is the diameter of the ellipse fitted to the most dense (red) part of the ratio_a - ratio_b density plot. The fit is a β distribution.

4.2 Muonic Background – Data set (1)

The following section, in which the muon-induced events are discussed, is part of [8]. Events coincident with the muon veto, called Pixel-Veto coincidences in the following, are recognized by analyzing the spectrum of time differences between the pixel event and veto event $\delta t = t(\text{pixel-event}) - t(\text{veto-event})$. This

spectrum can be seen in Figure 4.4 showing the time differences of all measured pixel events to veto events with $|\delta t| \leq 16 \mu\text{s}$ (Pixel-Veto coincidences: blue spectrum). The time window is chosen arbitrary large, with positive and negative values allowed, since the response time of the veto system and MMC detector system differ from each other. At $\delta t \approx 2.5 \mu\text{s}$ a peak is visible, which should include muon induced events. The same peak can be observed in the spectrum of time differences of pixel events to veto events, which are in addition coincidental to other pixel events and which are called Pixel-Pixel-Veto coincidences in the following (orange spectrum).

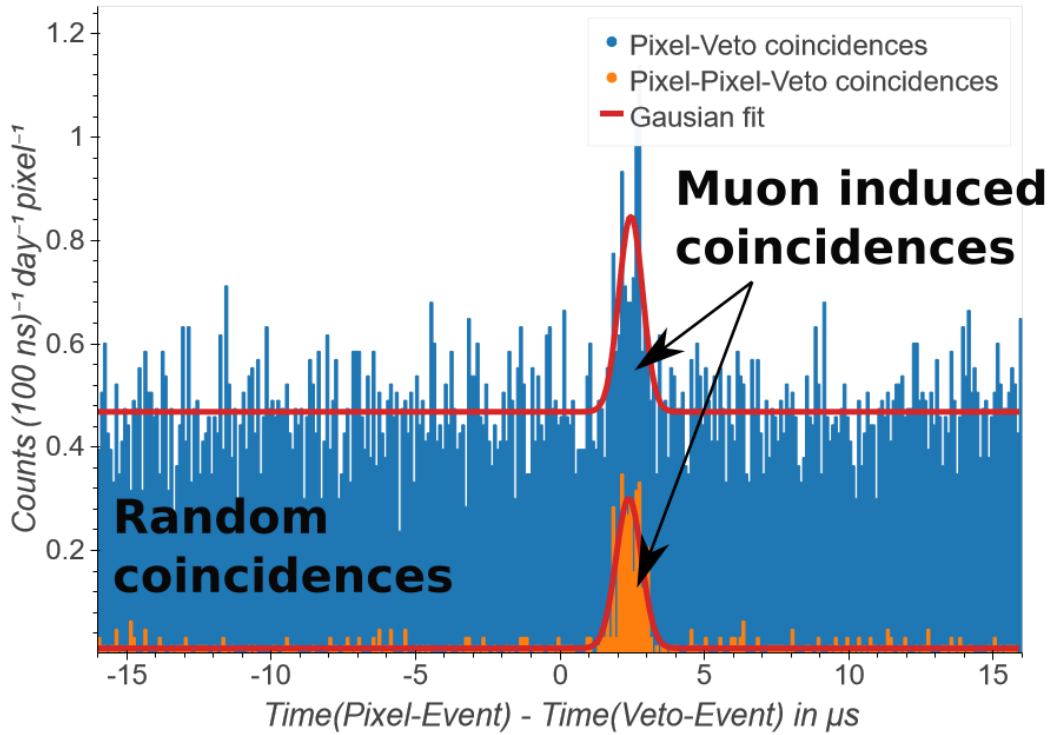


Figure 4.4: Spectrum of time differences δt between the pixel events and muon veto events $\delta t = t(\text{pixel-event}) - t(\text{veto-event})$. In blue, pixel events coincidental to the muon veto are shown. Events, also coincidental to other pixel events are shown in orange. At $\delta t \approx 2.5 \mu\text{s}$ a peak can be observed in both spectra corresponding to muon induced events. The flat spectrum corresponds to random coincidences between pixel events and muon veto. Taken from [8].

The peak of Pixel-Veto coincidences consists of $N = 242 \pm 20$ counts. This number is obtained by summing the raw number of counts in the 3σ range ($\sigma = (410 \pm 50) \text{ ns}$) after subtracting a flat background of (0.468 ± 0.005) counts $(100 \text{ ns})^{-1} \text{ day}^{-1} \text{ pixel}^{-1}$. The background and σ are determined by fitting a Gaussian plus a constant background to the spectrum of time differences.

The detection efficiency of the muon veto is estimated to about 56%. Combined with the detected number of muon induced events of $N = 242 \pm 20$ counts, a muon count rate of about (6.9 ± 0.5) counts $\text{day}^{-1} \text{pixel}^{-1}$ is estimated, which is about 14 times higher than $0.5 \text{ muons day}^{-1} \text{pixel}^{-1}$, which is expected for muons passing the pixels with a flux of $180 \text{ muons s}^{-1} \text{m}^{-2}$. Thus, this measurement suggests that each pixel can detect muons, which do not only hit the pixels directly, but also the substrate next to them. Accordingly, an effective area of about 14 times the pixel area can be identified, in which muons are registered by the pixels. This kind of events can be registered by multiple pixels simultaneously. Such events could either be caused by muons or secondary particles passing through an absorber, the corresponding sensor and the substrate next to the pixels, or by muons and secondary radiation passing only the substrate next to the pixels. In both cases, heat could diffuse to the pixels through the substrate. These types of event classes are defined as substrate events in the following.

The peak of the time difference spectrum of Pixel-Pixel-Veto coincidences (compare to the orange spectrum of Figure 4.4), which include muon induced substrate events, consists of 194 ± 12 counts. Thus, in this set-up, about $(80 \pm 8)\%$ of all muons generate coincidences among pixels. In this measurement, four detector pixels, with distances of about $120 \mu\text{m}$ to each other, were operated, which define the area of the active part of the detector chip. Corrected by the multiplicity of muon events, about $10 \text{ muons day}^{-1} \text{active detector chip area}^{-1}$ were detected, which corresponds to a muon flux for an area equal to 5 times the total pixel area ($5 \times 4 \text{ pixels} \times 0.5 \text{ muons day}^{-1} \text{pixel}^{-1}$).

As it can be seen in Figure 4.4, the signal to noise ratio of Pixel-Veto coincidences is about 0.3 in the 3σ -range around the peak, while the signal to noise ratio of Pixel-Pixel-Veto coincidences is about 6. Thus, in the following, the Pixel-Pixel-Veto coincidences will be used as a sample of substrate events in order to define a pulse shape analysis to cut substrate events from all events. Figure 4.5 shows the density of all measured events in the pulse shape parameter space $\text{FIR} = \frac{A_{\text{Filter}}}{A_{\text{Integral}}}$ and $\text{DTR} = \frac{A_{\text{Derivative}}}{A_{\text{Template}}}$. The orange dots in Figure 4.5 are visualizing the orange peak in the spectrum of Figure 4.4. The density of events is highest in an ellipse around $\text{FIR} \approx \text{DTR} \approx 1$, because these parameters are defined to be equal to one for events caused by the decay of ^{163}Ho . Muon induced substrate events are mostly located outside the ellipse.

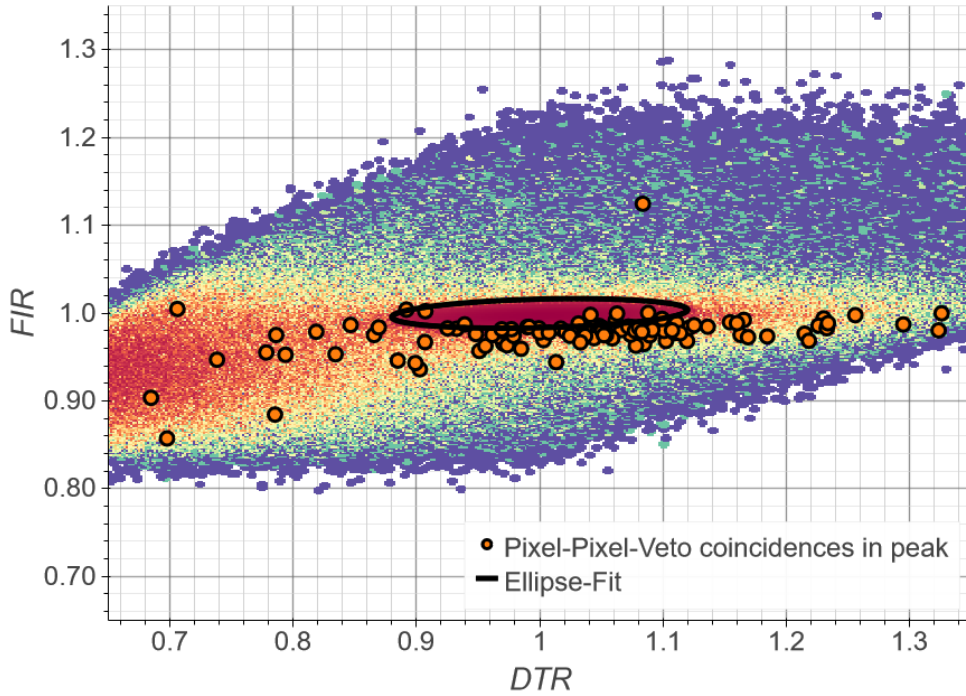


Figure 4.5: Density plot of events in the FIR vs. DTR parameter space. Muon related events are marked as orange dots and are mostly located in the surrounding of the ellipse defined by events due to the decay of ^{163}Ho in the pixels. Picture taken from [8].

Pixel-Veto coincidences outside the ellipses are selected and the spectrum of time differences of these events is investigated. The purple spectrum in Figure 4.6 shows these events. About 215 ± 15 events are located in the peak in this spectrum leading to a cut efficiency of about $(88.8 \pm 9.6)\%$ of recognizing muon induced (or substrate) events by their pulse shape.

In this data set, muon induced substrate events only result in energies of less than 950 eV, as seen in Figure 4.7, which shows the spectrum of deposited energies of muon induced events. The simulation of muons, which pass the detector, results in an expected number of counts of less than 0.6 direct hits of muons and secondary particles within 64 pixel-days in 0 keV to 4 keV. However, substrate events are not included in the simulation. Compared with about 215 measured muon induced substrate events¹ in 64 pixel-days, which can be caused by muons depositing energies in the substrate, it can be concluded, that this kind of events occurs with a much higher frequency than direct hits.

¹With and without coincidences among pixels.

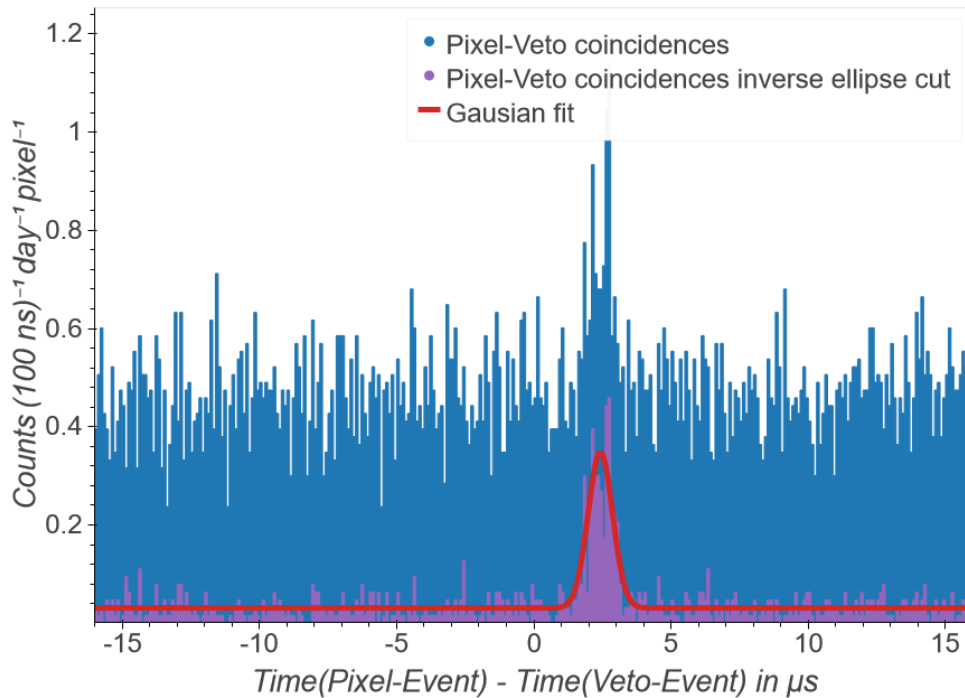


Figure 4.6: Spectrum of time differences δt between pixel events and muon veto events $\delta t = t(\text{pixel event}) - t(\text{veto event})$. The blue spectrum corresponds to all pixel events. The fraction of these events, which are outside of the ellipses is shown in purple. Taken from [8].

By extrapolating the observed muon induced spectrum by a flat distribution to the ROI and by considering the veto efficiency, a count rate of about $(7 \pm 2) \cdot 10^{-3} \text{ counts day}^{-1} \text{ pixel}^{-1}$ is expected in the ROI due to muons. This is much higher than the pile-up of the order of $10^{-6} \text{ counts day}^{-1} \text{ pixel}^{-1}$. In this conservative scenario, these events are not recognized by the coincidence with the muon veto, nor by pulse shape analysis or coincidence among MMC channels. The efficiency of the muon veto is assumed to be about 56%, the efficiency of the pulse shape analysis is about 89% and a muon generates coincidences among pixels in about 80% of all cases. Thus, the resulting count rate after all these cuts in the ROI is about $(7 \pm 7) \cdot 10^{-5} \text{ counts day}^{-1} \text{ pixel}^{-1}$.

4.3 Background Measurement - Data set (2)

The measured background spectrum, discussed in [7], is described in the following. Only unresolved pile-up and background events are expected above 3 keV. Because of this, events corresponding to energies above 3 keV are chosen from data acquired with ^{163}Ho -loaded pixels. The pulse height is limited to about 5 keV through due to ADC settings. After pulse shape analysis, four

events with energies between 3 keV and 5 keV were measured in 241 pixel-days of ^{163}Ho -loaded pixels. About 0.7 counts caused by unresolved pile-up events are expected in the same energy range with an exposure of 241 pixel-days, a ^{163}Ho activity of 1 Bq per pixel and a time resolution of $\tau_r = 500$ ns. By comparing to the expected pile-up spectrum, the probability, that one count out of these four events is due to pile-up is about 22%. Further, with a maximum likelihood analysis, the probability that two or more counts are caused by pile-up is calculated to be less than 0.2%.

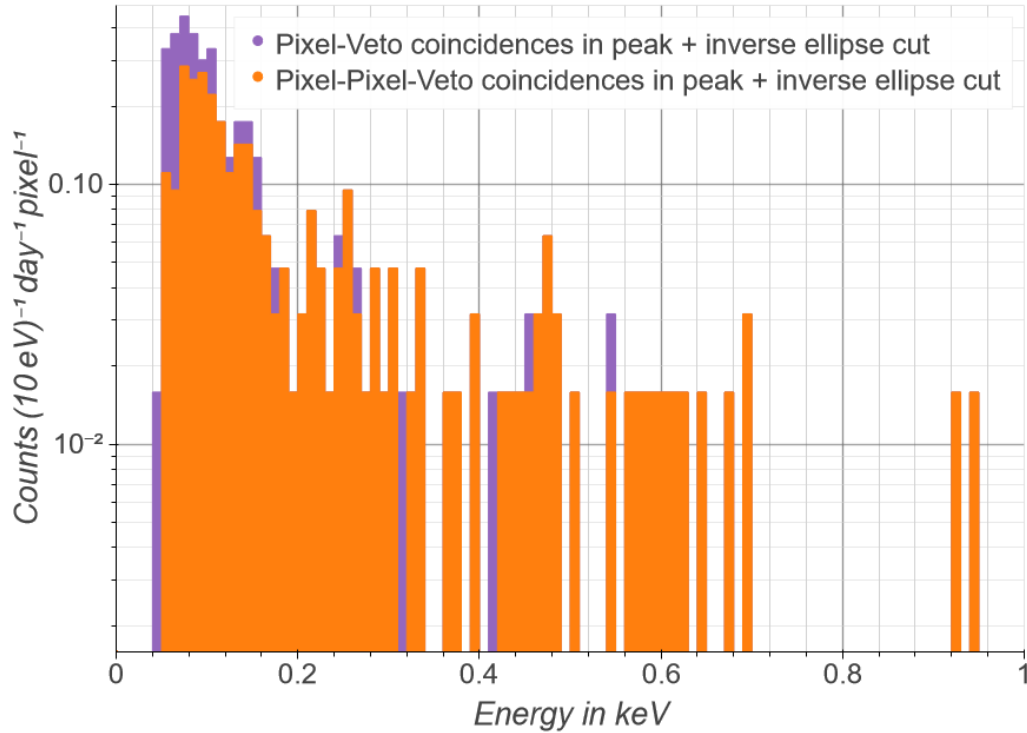


Figure 4.7: Spectrum of deposited energy of muon induced events. The highest measured energy is about 950 eV. Picture taken from [8].

For comparison, the expected pile-up spectrum and the energies of the measured events are shown in Figure 4.8. These events are more likely caused by different background sources. Assuming a flat background level, this results in a background level of $(8 \pm 4) \cdot 10^{-5}$ counts pixel $^{-1}$ day $^{-1}$ in the last 10 eV before Q_{EC} , which is one order higher than the pile-up in the ECHO-1k phase.

After the pulse shape analysis of data acquired by the non-loaded background pixels, no events with energies above 3 keV remain. Still, this is not in contradiction to the measurement with ^{163}Ho -loaded pixels, since the 95% confidence intervals for the mean of the Poisson distribution are $[0, 3.69)$ for no observa-

tions and [1.09, 10.24) for four counts. The possibility for a contamination of radionuclides implanted in the detector pixels in the ^{163}Ho implantation process is low. For example, $^{166\text{m}}\text{Ho}$ is considered as a critical co-implanted radionuclide. To achieve a background as high as 4 counts as described above, a fraction of $^{166\text{m}}\text{Ho}/^{163}\text{Ho} > 10^{-5}$ would be needed [63]. In the ECHo experiment a fraction of $^{166\text{m}}\text{Ho}/^{163}\text{Ho} < 10^{-9}$ is achieved, which is more than 4 orders of magnitudes smaller [61, 62].

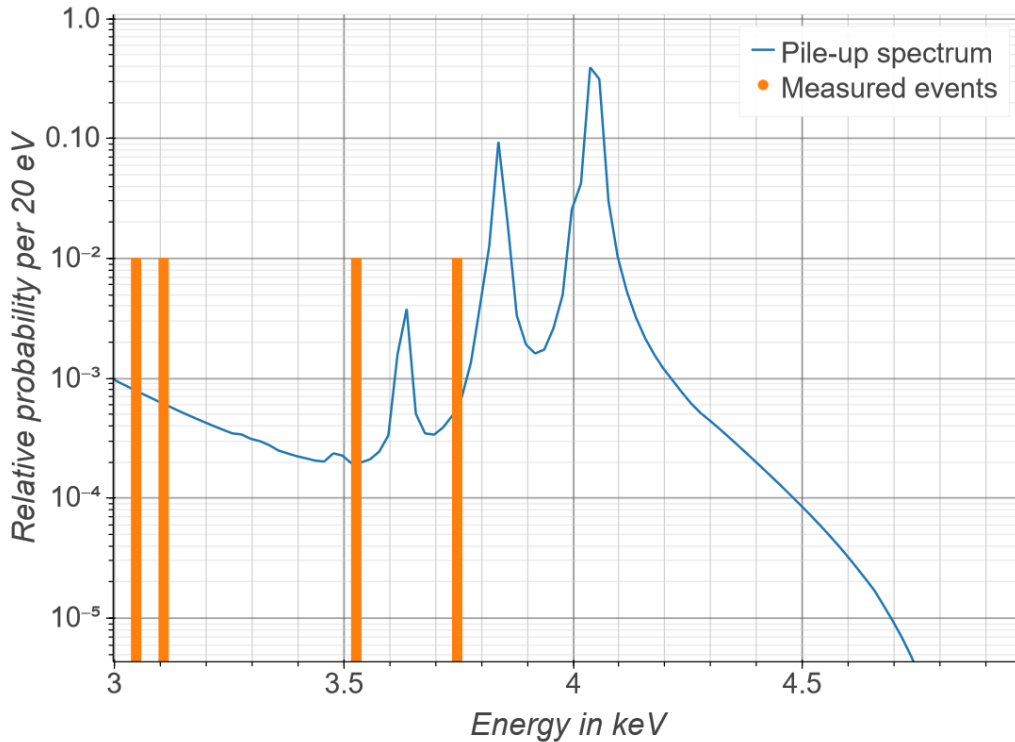


Figure 4.8: Normalized energy spectra of unresolved pile-up and measured events in 241 pixel-days. Taken from [7].

By combining the data acquired with the ^{163}Ho -loaded and unloaded pixels, the expected background level is about $(4 \pm 2) \cdot 10^{-5}$ counts pixel $^{-1}$ day $^{-1}$ in the ROI. Figure 4.9 shows the energy spectrum recorded by the background pixels after different analysis methods. Independently from the recorded background pixel, a spectrum similar to a ^{163}Ho EC spectrum is observed. Until know, this spectrum can neither be described by any simulations of natural radionuclides described in Section 3.3 or by muon caused events (compare to Section 3.2). If this spectrum is caused due to a ^{163}Ho contamination in the background pixels, the observed spectrum could correspond to an activity of about $30 \mu\text{Bq}$ of ^{163}Ho per pixel or about $6 \cdot 10^6$ ^{163}Ho atoms per pixel. An average activity per pixel is given, since the spectra acquired by different background pixels

look similar. The observed lines, which could represent the M lines around 2 keV of the ^{163}Ho EC, are slightly shifted to lower energies compared to the ^{163}Ho spectrum and the fraction of number of events of the N line ($300\text{ eV} < E < 600\text{ eV}$) to the number of events of the M line ($1700\text{ eV} < E < 2100\text{ eV}$) of 5.3 ± 1.0 is larger than expected from theory with 2.3. Note, that here an exponential background can be assumed, by fitting an exponential distribution to the spectra for energies below 200 eV, which however, is negligible above 300 eV. Both, the energy shift of the lines and the higher N/M-ratio, could be explained by a surface contamination of ^{163}Ho . In this case multiple particles could be emitted by the decay and not all have to deposit energy in the pixel. However, the observed spectrum could also be caused by a yet unknown background source. If the source of this spectrum has different origins, a background level of about $8 \cdot 10^{-5}$ counts pixel $^{-1}$ day $^{-1}$ can be assumed, since one event was measured between 2.5 keV and 3 keV in 241 pixel-days. The line at 1.49 keV could corresponds to aluminum X-rays.

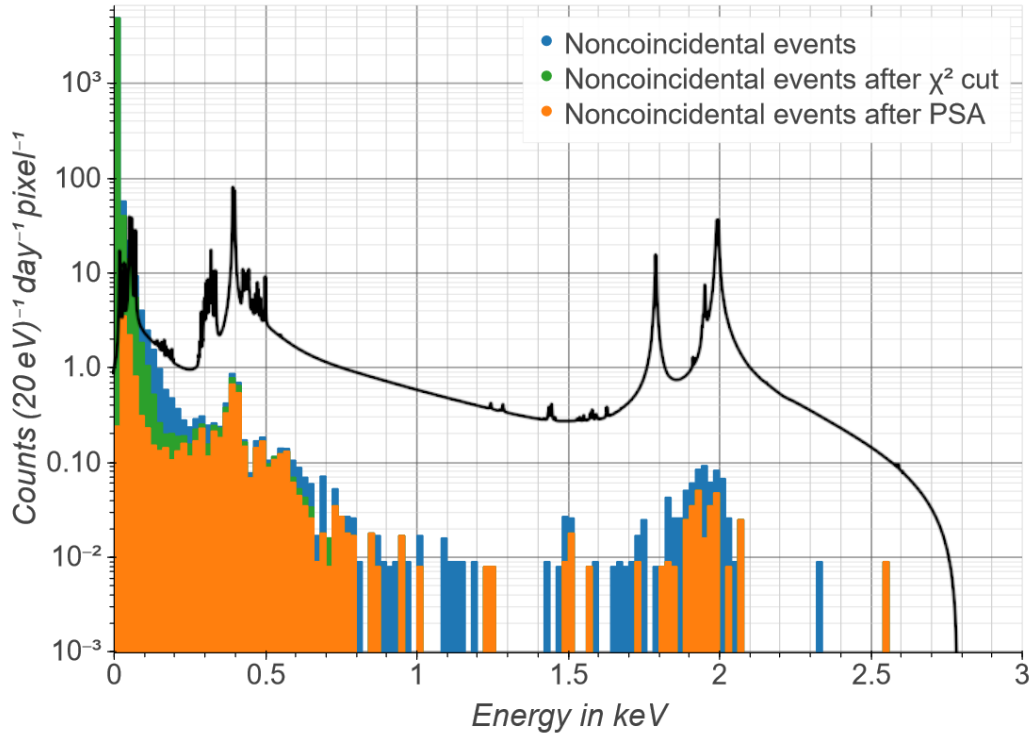


Figure 4.9: By background pixels recorded energy spectrum of non-coincidental events. The blue spectrum shows all measured events. The orange spectrum shows the actual background spectrum after applying the pulse shape analysis. The black line shows the theoretical ^{163}Ho EC spectrum. Figure taken from [7].

Chapter 5

Conclusion and Outlook

Different background sources in the ECHo experiment are studied in order to achieve a **background level** of the order of 10^{-6} **counts day⁻¹ pixel⁻¹** in the last 10 eV below Q_{EC} , which should be dominated by unresolved pile-up. This unresolved pile-up count rate corresponds to an unresolved pile-up fraction of $f_{\text{pu}} = 2 \cdot 1 \text{ Bq} \cdot 500 \text{ ns} = 10^{-6}$. Compared to [49] and by assuming a vanishing background, this pile-up fraction leads to a sensitivity on the effective electron neutrino mass of about 9 eV at 90% C.L. for the first phase of the ECHo experiment and to about 0.7 eV at 90% C.L. for future stages of the ECHo experiment. The effect of an additional background, which can not be neglected, can now be estimated by increasing the pile-up rate, such that the count rate in the ROI due to the unresolved pile-up is as high as the (measured) background level.

Thus, the effect on the sensitivity of a background of 10^{-4} **counts day⁻¹ pixel⁻¹** in the ROI can be estimated by an unresolved pile-up fraction of $f_{\text{pu}} = 10^{-4}$. With this pile-up fraction, the sensitivity decreases to about 11 eV for the first phase of the ECHo experiment and to about 1 eV for future stages of the experiment.

Pulse shape analysis Pulse shape analysis methods are developed to study the pulse shape of signals generated by the decay of ^{163}Ho in the pixel absorbers and by muons. It is possible to identify events related to the decay of ^{163}Ho in the absorbers and therefore, to remove pulses, whose shapes are different, like pulses caused by resolved pile-up, triggered noise or events, in which energy is deposited not (only) in the absorbers, but also in the sensor and in the substrate. Parameters like the pulse amplitude, the maximal derivative of the pulse, the integral of the pulse and response on filters are used to identify different pulse families.

The energy dependence of the pulse shape cuts need to be studied qualitatively in the future. To do this, pulses with different rise and decay times could be simulated and added to noise of measured signals. Thus, the cut and leakage efficiency depending on the pulse properties could be studied.

Unresolved pile-up In the first phase of the ECHo experiment, ECHo-1k, a count rate of about $3 \cdot 10^{-6}$ counts day⁻¹ pixel⁻¹ is expected due to unresolved pile-up. This includes a ¹⁶³Ho-activity of 1 Bq pixel⁻¹ and a time resolution of about $\tau_r = 500$ ns. For future stages of the ECHo experiment, with a ¹⁶³Ho-activity of 10 Bq pixel⁻¹ and a time resolution of about $\tau_r = 300$ ns for example, the pile-rate in the last 10 eV below the Q -value is expected to be about 10^{-4} counts day⁻¹ pixel⁻¹, while the signal count rate is about $6 \cdot 10^{-4}$ counts day⁻¹ pixel⁻¹.

Simulation of radionuclides Simulations of naturally occurring radionuclides in the detector materials show that relatively large levels of radioactivity of the order of 10 Bq kg⁻¹ or a few hundreds of μ Bq cm⁻² are needed to result in count rates in the ROI as high as the count rate due to the unresolved pile-up. With upper limits of concentrations of naturally occurring radionuclides in materials used in the ECHo-1k phase, which result from screening measurements, an expected energy spectrum recorded by the detector pixels is simulated and results in a count rate of about $(7 \pm 1) \cdot 10^{-6}$ counts day⁻¹ pixel⁻¹ in the ROI, mainly due to radionuclides in the circuit board.

For the future stages of the ECHo experiment, different materials (Kapton) are foreseen as material for circuit boards. This should reduce the background due to natural radionuclides of about 90%. Screening measurements of future used materials should be performed and used as input for simulations of naturally occurring radionuclides in the materials to determine the influence of these materials in the next stages of the ECHo experiment.

Background measurement A measurement with ¹⁶³Ho-loaded and -unloaded (background) pixels was performed and analyzed by using pulse shape discrimination methods. In 241 pixel-days, four events with energies above 3 keV are measured by ¹⁶³Ho-loaded pixels resulting in a count rate of $(8 \pm 4) \cdot 10^{-5}$ counts day⁻¹ pixel⁻¹ in the ROI. Most likely, these events are not caused by unresolved pile-up. The background pixels did not measure any events with energies above 3 keV in 241 pixel-days, but recorded a ¹⁶³Ho EC-like spectrum, which could correspond to a ¹⁶³Ho contamination of about 30μ Bq pixel⁻¹.

Future high statistics measurements (long measurement times) need to be analyzed to gain a precise knowledge of the background spectrum. In addition, the sensitive energy range will be extended to study possible structures above 5 keV.

Simulation of muons Muons passing the detector chip are simulated and predict a count rate in the ROI of about $(2.2 \pm 0.1) \cdot 10^{-5} \text{ counts day}^{-1} \text{ pixel}^{-1}$. This rate only includes muons and secondary radiation passing directly the detector pixels and does not include substrate events. With pulse shape analysis, this rate should be reduced by more than 90%, since the particles are mostly not stopped in the pixels and can further be reduced by the use a muon veto.

Measurement with muon veto A measurement including the operation of an active muon veto recorded a count rate of $(7 \pm 2) \cdot 10^{-3} \text{ counts day}^{-1} \text{ pixel}^{-1}$ in the ROI due to muon induced substrate events. This background should be reduced to $(7 \pm 7) \cdot 10^{-5} \text{ counts day}^{-1} \text{ pixel}^{-1}$ with pulse shape analysis, the use of a muon veto and the analysis of trigger time information.

Bibliography

- [1] F. Mantegazzini *et al.*, “Multichannel read-out for arrays of metallic magnetic calorimeters,” *Journal of Instrumentation* **16** no. 08, (2021) P08003. <http://dx.doi.org/10.1088/1748-0221/16/08/P08003>.
- [2] F. Mantegazzini, “Development and characterisation of high-resolution metallic magnetic calorimeter arrays for the echo neutrino mass experiment,” 2021. <http://www.ub.uni-heidelberg.de/archiv/30250>.
- [3] F. Mantegazzini *et al.* *Journal of Instrumentation* (submitted) .
- [4] C. Velte, “Measurement of high energy resolution and high statistics ^{163}Ho electron capture spectrum for the echo experiment,” 2020. <http://www.ub.uni-heidelberg.de/archiv/27340>.
- [5] C. Velte *et al.*, “High-resolution and low-background ^{163}Ho spectrum: interpretation of the resonance tails,” *The European Physical Journal C* **79** (2019) 1026. <https://doi.org/10.1140/epjc/s10052-019-7513-x>.
- [6] R. Hammann *et al.*, “Data reduction for a calorimetrically measured ^{163}Ho spectrum of the ECHO-1k experiment,” 2021.
- [7] A. Göggelmann *et al.*, “Study of naturally occurring radionuclides in the ECHO set-up,” *The European Physical Journal C* **82** (2022) 139. <https://doi.org/10.1140/epjc/s10052-022-10112-7>.
- [8] A. Göggelmann *et al.*, “Study of muon-induced background in mmc detector arrays for the echo experiment,” *The European Physical Journal C* **81** (2021) 363. <https://doi.org/10.1140/epjc/s10052-021-09148-y>.
- [9] W. Pauli, “Offener Brief an die Gruppe der Radioaktiven bei der Gauvereine-Tagung zu Tübingen.” Open letter, 1930.

- [10] C. L. Cowan *et al.*, “Detection of the free neutrino: a confirmation,” *Science* **124** no. 3212, (1956) 103–104, <https://www.science.org/doi/pdf/10.1126/science.124.3212.103>. <https://www.science.org/doi/abs/10.1126/science.124.3212.103>.
- [11] R. Davis, “A review of the homestake solar neutrino experiment,” *Progress in Particle and Nuclear Physics* **32** (1994) 13–32. <https://www.sciencedirect.com/science/article/pii/0146641094900043>.
- [12] **SNO Collaboration** Collaboration, Q. R. Ahmad *et al.*, “Direct evidence for neutrino flavor transformation from neutral-current interactions in the sudbury neutrino observatory,” *Phys. Rev. Lett.* **89** (2002) 011301. <https://link.aps.org/doi/10.1103/PhysRevLett.89.011301>.
- [13] **Super-Kamiokande Collaboration** Collaboration, S. Fukuda *et al.*, “Constraints on neutrino oscillations using 1258 days of super-kamiokande solar neutrino data,” *Phys. Rev. Lett.* **86** (2001) 5656–5660. <https://link.aps.org/doi/10.1103/PhysRevLett.86.5656>.
- [14] F. Capozzi *et al.*, “Current unknowns in the three-neutrino framework,” *Progress in Particle and Nuclear Physics* **102** (2018) 48–72. <https://www.sciencedirect.com/science/article/pii/S0146641018300383>.
- [15] P. de Salas *et al.*, “Status of neutrino oscillations 2018: 3σ hint for normal mass ordering and improved cp sensitivity,” *Physics Letters B* **782** (2018) 633–640. <https://www.sciencedirect.com/science/article/pii/S0370269318304672>.
- [16] KATRIN Collaboration, “Direct neutrino-mass measurement with sub-electronvolt sensitivity,” *Nature Physics* **18** (2022) 160–166. <https://doi.org/10.1038/s41567-021-01463-1>.
- [17] Planck Collaboration, “Planck 2018 results - xiii. cosmological parameters,” *A&A* **641** (2020) A6. <https://doi.org/10.1051/0004-6361/201833910>.
- [18] **GERDA Collaboration** Collaboration, M. Agostini *et al.*, “Final results of gerda on the search for neutrinoless double- β decay,” *Phys. Rev. Lett.* **125** (2020) 252502. <https://link.aps.org/doi/10.1103/PhysRevLett.125.252502>.

- [19] **Particle Data Group** Collaboration, P. Zyla *et al.*, “Review of Particle Physics,” *PTEP* **2020** no. 8, (2020) 083C01. <https://doi.org/10.1093/ptep/ptaa104>.
- [20] K. S. Hirata *et al.*, “Real-time, directional measurement of ^8B solar neutrinos in the Kamiokande II detector,” *Phys. Rev. D* **44** (1991) 2241–2260. <https://link.aps.org/doi/10.1103/PhysRevD.44.2241>.
- [21] V. Gavrin *et al.*, “Sage: The soviet-american gallium solar neutrino experiment,” *Nuclear Physics B - Proceedings Supplements* **28** no. 1, (1992) 75–81. <https://www.sciencedirect.com/science/article/pii/092056329290149M>.
- [22] D. Vignaud, “The gallex solar neutrino experiment,” *Nuclear Physics B - Proceedings Supplements* **60** no. 3, (1998) 20–29. <https://www.sciencedirect.com/science/article/pii/S0920563297004982>.
- [23] M. Altmann *et al.*, “Complete results for five years of gno solar neutrino observations,” *Physics Letters B* **616** no. 3, (2005) 174–190. <https://www.sciencedirect.com/science/article/pii/S0370269305005149>.
- [24] Y. Suzuki, “The super-kamiokande experiment,” *The European Physical Journal C* **79** no. 4, (2019) 298. <https://doi.org/10.1140/epjc/s10052-019-6796-2>.
- [25] A. Bellerive *et al.*, “The sudbury neutrino observatory,” *Nuclear Physics B* **908** (2016) 30–51. <https://www.sciencedirect.com/science/article/pii/S0550321316300736>. Neutrino Oscillations: Celebrating the Nobel Prize in Physics 2015.
- [26] M. Decowski, “Kamland’s precision neutrino oscillation measurements,” *Nuclear Physics B* **908** (2016) 52–61. <https://www.sciencedirect.com/science/article/pii/S0550321316300529>. Neutrino Oscillations: Celebrating the Nobel Prize in Physics 2015.
- [27] G. Ranucci *et al.*, “Overview and accomplishments of the borexino experiment,” *Journal of Physics: Conference Series* **675** no. 1, (2016) 012036. <https://doi.org/10.1088/1742-6596/675/1/012036>.
- [28] B. T. Cleveland *et al.*, “Measurement of the solar electron neutrino flux with the homestake chlorine detector,” <https://doi.org/10.1086/305343>.

- [29] **Super-Kamiokande Collaboration** Collaboration, K. Abe *et al.*, “Atmospheric neutrino oscillation analysis with external constraints in super-kamiokande i-iv,” *Phys. Rev. D* **97** (2018) 072001.
<https://link.aps.org/doi/10.1103/PhysRevD.97.072001>.
- [30] A. Collaboration, “Measuring the atmospheric neutrino oscillation parameters and constraining the 3+1 neutrino model with ten years of antares data,” 2019.
- [31] **IceCube Collaboration** Collaboration, M. G. Aartsen *et al.*, “Measurement of atmospheric neutrino oscillations at 6–56 gev with icecube deepcore,” *Phys. Rev. Lett.* **120** (2018) 071801.
<https://link.aps.org/doi/10.1103/PhysRevLett.120.071801>.
- [32] **K2K Collaboration** Collaboration, M. H. Ahn *et al.*, “Measurement of neutrino oscillation by the k2k experiment,” *Phys. Rev. D* **74** (2006) 072003. <https://link.aps.org/doi/10.1103/PhysRevD.74.072003>.
- [33] **MINOS+ Collaboration** Collaboration, P. Adamson *et al.*, “Precision constraints for three-flavor neutrino oscillations from the full MINOS+ and minos dataset,” *Phys. Rev. Lett.* **125** (2020) 131802.
<https://link.aps.org/doi/10.1103/PhysRevLett.125.131802>.
- [34] **T2K Collaboration** Collaboration, K. Abe *et al.*, “Observation of electron neutrino appearance in a muon neutrino beam,” *Phys. Rev. Lett.* **112** (2014) 061802.
<https://link.aps.org/doi/10.1103/PhysRevLett.112.061802>.
- [35] **NOvA Collaboration** Collaboration, M. A. Acero *et al.*, “First measurement of neutrino oscillation parameters using neutrinos and antineutrinos by nova,” *Phys. Rev. Lett.* **123** (2019) 151803.
<https://link.aps.org/doi/10.1103/PhysRevLett.123.151803>.
- [36] **Daya Bay Collaboration** Collaboration, D. Adey *et al.*, “Improved measurement of the reactor antineutrino flux at daya bay,” *Phys. Rev. D* **100** (2019) 052004.
<https://link.aps.org/doi/10.1103/PhysRevD.100.052004>.
- [37] **RENO Collaboration** Collaboration, G. Bak *et al.*, “Measurement of reactor antineutrino oscillation amplitude and frequency at reno,” *Phys. Rev. Lett.* **121** (2018) 201801.
<https://link.aps.org/doi/10.1103/PhysRevLett.121.201801>.

- [38] **Double Chooz Collaboration** Collaboration, H. de Kerret *et al.*, “Double chooz θ_{13} measurement via total neutron capture detection,” *Nature Physics* **16** (2020) 558–564. <https://doi.org/10.1038/s41567-020-0831-y>.
- [39] S. Alam *et al.*, “Completed sdss-iv extended baryon oscillation spectroscopic survey: Cosmological implications from two decades of spectroscopic surveys at the apache point observatory,” *Phys. Rev. D* **103** (2021) 083533. <https://link.aps.org/doi/10.1103/PhysRevD.103.083533>.
- [40] D. M. Scolnic *et al.*, “The complete light-curve sample of spectroscopically confirmed SNe ia from pan-STARRS1 and cosmological constraints from the combined pantheon sample,” *The Astrophysical Journal* **859** no. 2, (2018) 101. <https://doi.org/10.3847/1538-4357/aab9bb>.
- [41] J. Froustey, C. Pitrou, and M. C. Volpe, “Neutrino decoupling including flavour oscillations and primordial nucleosynthesis,” *Journal of Cosmology and Astroparticle Physics* **2020** no. 12, (2020) 015–015. <https://doi.org/10.1088/1475-7516/2020/12/015>.
- [42] J. J. Bennett *et al.*, “Towards a precision calculation of the effective number of neutrinos n_{eff} in the standard model. partii. neutrino decoupling in the presence of flavour oscillations and finite-temperature QED,” *Journal of Cosmology and Astroparticle Physics* **2021** no. 04, (2021) 073. <https://doi.org/10.1088/1475-7516/2021/04/073>.
- [43] J. Birrell, C. T. Yang, and J. Rafelski, “Relic neutrino freeze-out: Dependence on natural constants,” *Nuclear Physics B* **890** (2015) 481–517. <https://www.sciencedirect.com/science/article/pii/S0550321314003642>.
- [44] E. D. Valentino, A. Melchiorri, and J. Silk, “Cosmological constraints in extended parameter space from the planck 2018 legacy release,” *Journal of Cosmology and Astroparticle Physics* **2020** no. 01, (2020) 013–013. <https://doi.org/10.1088/1475-7516/2020/01/013>.
- [45] D. Collaboration, “Dark energy survey year 3 results: Cosmological constraints from galaxy clustering and weak lensing,” 2021. <https://arxiv.org/abs/2105.13549>.
- [46] J. Bonn *et al.*, “The mainz neutrino mass experiment,” *Nuclear Physics B - Proceedings Supplements* **91** no. 1, (2001) 273–279. <https://www>.

sciencedirect.com/science/article/pii/S0920563200009518.
Neutrino 2000.

- [47] V. Lobashev *et al.*, “Direct search for neutrino mass and anomaly in the tritium beta-spectrum: Status of ”troitsk neutrino mas” experiment,” *Nuclear Physics B - Proceedings Supplements* **91** no. 1, (2001) 280–286. <https://www.sciencedirect.com/science/article/pii/S092056320000952X>. Neutrino 2000.
- [48] B. Monreal and J. A. Formaggio, “Relativistic cyclotron radiation detection of tritium decay electrons as a new technique for measuring the neutrino mass,” *Phys. Rev. D* **80** (2009) 051301. <https://link.aps.org/doi/10.1103/PhysRevD.80.051301>.
- [49] L. Gastaldo *et al.*, “The electron capture in ^{163}Ho experiment – echo,” *The European Physical Journal Special Topics* **226** no. 8, (2017) 1623–1694. <https://doi.org/10.1140/epjst/e2017-70071-y>.
- [50] B. Alpert *et al.*, “HOLMES,” *The European Physical Journal C* **75** no. 3, (2015) 112. <https://doi.org/10.1140/epjc/s10052-015-3329-5>.
- [51] M. P. Croce *et al.*, “Development of Holmium-163 Electron-Capture Spectroscopy with Transition-Edge Sensors,” *Journal of Low Temperature Physics* **184** no. 3, (2015) 958–968. <https://doi.org/10.1007/s10909-015-1451-2>.
- [52] A. Fleischmann *et al.*, “Metallic magnetic calorimeters,” *AIP Conference Proceedings* **1185** no. 1, (2009) 571–578. <https://aip.scitation.org/doi/abs/10.1063/1.3292407>.
- [53] S. Kempf *et al.*, “Physics and applications of metallic magnetic calorimeters,” *Journal of Low Temperature Physics* **193** no. 3, (2018) 365–379. <https://doi.org/10.1007/s10909-018-1891-6>.
- [54] M. Braß and M. W. Haverkort, “*Ab initio* calculation of the electron capture spectrum of ^{163}Ho : Auger–Meitner decay into continuum states,” *New J. Phys.* **22** no. 9, (2020) 093018, [arXiv:2002.05989](https://arxiv.org/abs/2002.05989) [nucl-th].
- [55] M. Braß *et al.*, “*Ab initio* calculation of the calorimetric electron-capture spectrum of ^{163}Ho : Intra-atomic decay into bound states,” *Phys. Rev. C* **97** (2018) 054620. <https://link.aps.org/doi/10.1103/PhysRevC.97.054620>.

- [56] S. Eliseev *et al.*, “Direct measurement of the mass difference of ^{163}Ho and ^{163}Dy solves the q -value puzzle for the neutrino mass determination,” *Phys. Rev. Lett.* **115** (2015) 062501.
<https://link.aps.org/doi/10.1103/PhysRevLett.115.062501>.
- [57] F. Mantegazzini *et al.* *Nuclear Instruments and Methods in Physics Research Section A: Accelerators, Spectrometers, Detectors and Associated Equipment* (will be submitted) .
- [58] C. Enss and S. Hunklinger, *Tieftemperaturphysik*. Springer Berlin Heidelberg, Berlin, Heidelberg, 2000.
- [59] A. Göggelmann *et al.*, “A pulse shape analysis for the ECHO experiment,” *attached manuscript* .
- [60] J. Engle *et al.*, “Evaluation of ^{163}Ho production options for neutrino mass measurements with microcalorimeter detectors,” *Nuclear Instruments and Methods in Physics Research Section B: Beam Interactions with Materials and Atoms* **311** (2013) 131–138. <https://www.sciencedirect.com/science/article/pii/S0168583X13006459>.
- [61] H. Dorrer *et al.*, “Production, isolation and characterization of radiochemically pure ^{163}Ho samples for the echo-project,” *Radiochimica Acta* **106** no. 7, (2018) 535–547.
<https://doi.org/10.1515/ract-2017-2877>.
- [62] T. Kieck *et al.*, “Highly efficient isotope separation and ion implantation of ^{163}Ho for the echo project,” *Nuclear Instruments and Methods in Physics Research Section A: Accelerators, Spectrometers, Detectors and Associated Equipment* **945** (2019) 162602. <https://www.sciencedirect.com/science/article/pii/S016890021931109X>.
- [63] S. Scholl, “Background analysis and reduction for the ECHO experiment,” *Journal of Physics: Conference Series* **718** (2016) 062051.
<https://doi.org/10.1088%2F1742-6596%2F718%2F6%2F062051>.
- [64] S. Scholl, A. Zschocke, and J. Jochum, “Background simulations for the ECHO experiment,” *Journal of Physics: Conference Series* **888** (2017) 012225.
<https://doi.org/10.1088%2F1742-6596%2F888%2F1%2F012225>.
- [65] S. Taylor, “Abundance of chemical elements in the continental crust: a new table,” *Geochimica et Cosmochimica Acta* **28** no. 8, (1964) 1273 – 1285.

<http://www.sciencedirect.com/science/article/pii/S0168900220303697>

- [66] D. Budjas *et al.*, “Highly sensitive gamma-spectrometers of gerda for material screening: Part i,” arXiv:0812.0723 [physics.ins-det].
<https://arxiv.org/abs/0812.0723>.
- [67] D. Budjas *et al.*, “Highly sensitive gamma-spectrometers of gerda for material screening: Part ii,” arXiv:0812.0768 [physics.ins-det].
<https://arxiv.org/abs/0812.0768>.
- [68] J. Kaizer, S. Nisi, and P. Povinec, “Radiopurity measurements of aluminum, copper and selenium materials for underground experiments and mass spectrometry development,” *Journal of Radioanalytical and Nuclear Chemistry* **322** no. 3, (2019) 1447–1454.
<https://doi.org/10.1007/s10967-019-06857-3>.
- [69] ILIAS, “Ilias database on radiopurity of materials.”
<http://radiopurity.in2p3.fr/>.
- [70] National Research Council (US) Committee on Health Risks of Exposure to Radon (BEIR VI), *Health Effects of Exposure to Radon*. National Academics Press (US), Washington (DC), 1999.
- [71] R. Bunker *et al.*, “Evaluation and mitigation of trace 210pb contamination on copper surfaces,” *Nuclear Instruments and Methods in Physics Research Section A: Accelerators, Spectrometers, Detectors and Associated Equipment* **967** (2020) 163870. <https://www.sciencedirect.com/science/article/pii/S0168900220303697>.
- [72] S. Chu, L. Ekström, and R. Firestone, “The lund/lbnl nuclear data search,” <http://nucleardata.nuclear.lu.se/toi/>.
- [73] *Naturally Occurring Radioactive Materials (NORM IV) - Proceedings of an International Conference held in Szczyrk, Poland, 17-21 May 2004*. No. 1472 in TECDOC Series. INTERNATIONAL ATOMIC ENERGY AGENCY, Vienna, 2005.
- [74] J. P. McBride *et al.*, “Radiological impact of airborne effluents of coal and nuclear plants,” *Science* **202** no. 4372, (1978) 1045–1050,
<https://science.sciencemag.org/content/202/4372/1045.full.pdf>.
<https://science.sciencemag.org/content/202/4372/1045>.

- [75] T. R. Ajayi *et al.*, “Natural radioactivity and trace metals in crude oils: implication for health,” *Environmental Geochemistry and Health* **31** no. 1, (2009) 61–69. <https://doi.org/10.1007/s10653-008-9155-z>.
- [76] D. Reyna, “A Simple parameterization of the cosmic-ray muon momentum spectra at the surface as a function of zenith angle.” 4, 2006.
- [77] P. Shukla and S. Sankrith, “Energy and angular distributions of atmospheric muons at the earth,” *International Journal of Modern Physics A* **33** no. 30, (2018) 1850175, <https://doi.org/10.1142/S0217751X18501750>.
<https://doi.org/10.1142/S0217751X18501750>.
- [78] L. Landau, “On the energy loss of fast particles by ionization,” *J. Phys. (USSR)* **8** (1944) 201–205.
- [79] H. Bichsel, “Straggling in Thin Silicon Detectors,” *Rev. Mod. Phys.* **60** (1988) 663–699.
- [80] D. Wilkinson, “Ionization energy loss by charged particles part i. the landau distribution,” *Nuclear Instruments and Methods in Physics Research Section A: Accelerators, Spectrometers, Detectors and Associated Equipment* **383** no. 2, (1996) 513 – 515. <http://www.sciencedirect.com/science/article/pii/S0168900296007747>.
- [81] S. Agostinelli *et al.*, “Geant4—a simulation toolkit,” *Nuclear Instruments and Methods in Physics Research Section A: Accelerators, Spectrometers, Detectors and Associated Equipment* **506** no. 3, (2003) 250 – 303. <http://www.sciencedirect.com/science/article/pii/S0168900203013688>.
- [82] C. R. A. Augusto *et al.*, “VARIATIONS OF THE MUON FLUX AT SEA LEVEL ASSOCIATED WITH INTERPLANETARY ICMEs AND COROTATING INTERACTION REGIONS,” *The Astrophysical Journal* **759** no. 2, (2012) 143. <https://doi.org/10.1088/0004-637x/759/2/143>.

Appendix

Non-submitted manuscripts

A pulse shape analysis for the ECHo experiment

A. Göggelmann^{a,1}, J. Jochum¹, L. Gastaldo², F. Mantegazzini², A. Barth²,
 R. Hammann²

¹Physics Institute, University of Tübingen, Tübingen, Germany

²Kirchhoff Institute for Physics, Heidelberg University, Heidelberg, Germany

Received: date / Accepted: date

1 Pulse shape study

Data acquired in two independent measurements between Dec 2019 and May 2020 are analyzed and discussed here. This data is received by five pixels, each loaded with about 1 Bq of ^{163}Ho resulting in about 241 pixel-days of data of ^{163}Ho events. Actually, more pixels were operated within the measurements but will not be discussed here. However, the trigger time information of events received by the others pixels will be used. In order to separate events caused by particles, which deposit their complete energies in the pixels, from events caused by particles not fully stopped in the pixels, signals due to the decay of ^{163}Ho are analyzed first. The signal pulse shape can be described by several parameters and are calibrated by using ^{163}Ho caused events, which correspond to events due to particles fully stopped in the pixels.

1.1 Pulse shape parameters

The pulse shape analysis is based on the analysis developed to recognize muon induced events [1]. Five parameters are obtained from each pulse, its integral, rise time and amplitude on the one hand and on the other hand the pulse is compared to a template and correlated with the same template. The signals correspond to time traces with a length of about 2 ms. These traces include two parts, the pre-trigger, which corresponds to the first quarter part of a trace, and the actual triggered signals. In the following, only the second quarter of a signal will be considered as a pulse in order to shorten the pile-up window.

Template fitting

The template signal is obtained by averaging one thousand to five thousand signals with amplitudes corresponding to energies of the ^{163}Ho -MI line. This is done for each pixel and each measurement day. The template signal of a ^{163}Ho loaded pixel is also used as a template signal for the background pixel of the same channel. An exemplary template signal is shown as the blue solid curve in Figure 1. The actual used part, the second quarter of the template signal, is shown as the solid orange line. In the following, only this part will be considered, when talking about the template pulse. The template pulse is fitted to each pulse using the χ^2 method of varying the amplitude of the template. From this, the reduced χ^2 (i.e. χ^2/dof^{-1}), which describes the similarity of the template pulse and each signal pulse, is obtained. In order to recognize pile-up within the length of the template pulse ($\delta t \approx 500 \mu\text{s}$), the template's tail, the last quarter of the template pulse (the green dotted part), is also fitted to each pulse resulting in the amplitude A_{Template} of the fit. This method is sensitive to the overall pulse shape, but mainly to the falling edge of the pulses.

Filtering

The beginning of the template pulse is used to build a new time trace, called filter (red dotted line in Figure 1). This short length is chosen to become insensitive to pile-up on the falling edge of the pulses. Each pulse is correlated with this filter (so called matched filtering). The amplitude of the response function A_{Filter} describes mainly the area below the pulse around the rising edge (red area). This method is sensitive to the overall pulse shape around the rising edge.

Differentiation

^ae-mail: alexander.goeggelmann@uni-tuebingen.de

The derivative of the pulses smoothed by using a moving average filter results in the maximum of the derivative of the smoothed pulses $A_{\text{Derivative}}$ (compare to the red curve in Figure 1). This method is sensitive to pile-up with short time differences and to other effects, which could change the rise time.

Integrating

The area A_{Integral} under the pulses is calculated. This method is sensitive to pile-up with large time differences and to other effects which could change the mean decay time (compare to the orange area in Figure 1).

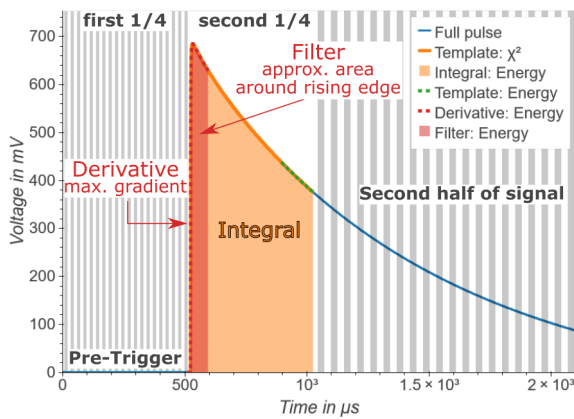


Fig. 1: An exemplary template signal. The different colors show the different parts of the time trace used in the different analysis methods. A full template signal is shown as the blue solid line. The second quarter of the signal (orange line) shows the template pulse and is fitted to each pulse to obtain the reduced χ^2 . The tail of the template pulse (the last quarter, green dotted curve) is fitted to each pulse to obtain the amplitude of the fit. The first part of the template around the rising edge (red dotted curve) is correlated with each pulse, resulting mainly in the area under the pulse around the rising edge (red area). The derivative of the smoothed pulses are calculated to obtain the maximum gradient. Last, the area under the pulses (orange area) is calculated.

Each of the four methods is differently sensitive to the pulse shape. In order to distinguish between signals caused by the ^{163}Ho EC decay in the absorbers or by particles absorbed in the absorbers and signals caused by other processes, the ratio of the pulse shape parameters are considered. These ratios are the same for all energies for events caused by similar processes, but different for different processes. For pulses due to the ^{163}Ho

EC decay or similar, these ratios are set to 1. Also, the reduced χ^2 is equal to 1 for these type of pulses.

1.2 Pulse shape cuts

Reduced χ^2

^{163}Ho decays result in events with mostly $\chi^2 \text{dof}^{-1} < 2$ (compare to Figure 2). Thus, a χ^2 range cut is the starting point for the following pulse shape analysis. A cut of $\chi^2 \text{dof}^{-1} < 2$ can be defined to describe events, which are similar to events caused by the decay of ^{163}Ho .

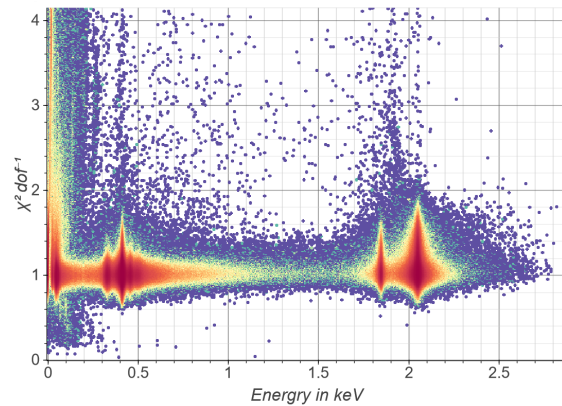


Fig. 2: Reduced χ^2 against the deposited energy of events of ^{163}Ho -loaded pixels. The ^{163}Ho lines can be observed around $\chi^2 \text{dof}^{-1} \approx 1$.

Time differences

We observe that the spectrum of time differences between two pixel events decays exponential until $\delta t \approx 2 \mu\text{s}$ and is flat for larger time differences (compare to Figure 3). The spectrum includes events of the five mentioned pixels which can also be coincidental to other pixel events of all other channels. These type of events are most probably caused by electromagnetic radiation coupling in the readout chain of the detectors as described in the next chapter. A time difference condition of $\delta t > 4 \mu\text{s}$ can be defined to define non-coincidental events. These events are shown as the orange spectrum in Figure 4. Using this non-coincidence cut, most of the events with $\chi^2 \text{dof}^{-1} > 2$ are reduced compared to all events (see Figure 4).

Ellipses

Four methods are introduced in Chapter 1.3, fitting a **T**emplate, **F**iltering, **I**ntegrating and **D**ifferentiation, to reconstruct the deposited energy are introduced in Chapter 1.3. With these four energies, six ratios can be

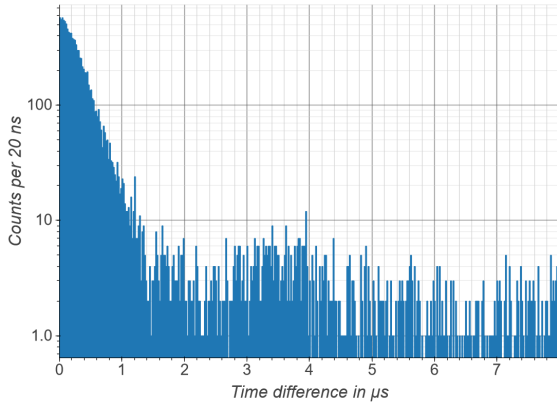


Fig. 3: Distribution of time differences between two pixel events for all pixels. The distribution is almost constant for high time differences and increases strongly for low time differences starting at around $1.5 \mu\text{s}$.

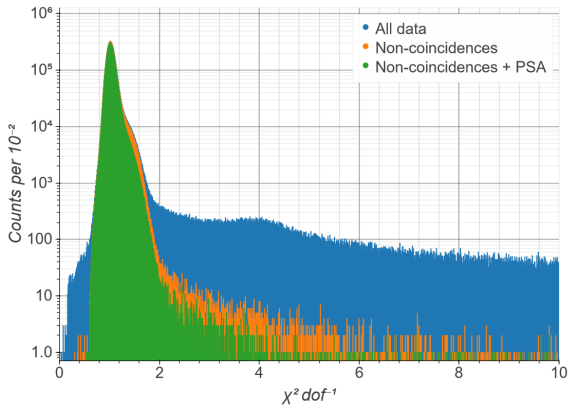


Fig. 4: Distribution of the reduced $\chi^2 = \chi^2 \text{dof}^{-1}$ of events of ^{163}Ho -loaded pixels. The blue spectrum shows all data, the orange spectrum data, which is not coincidental ($\delta t > 4 \mu\text{s}$) to other events and the fraction of these events, which remain after the pulse shape analysis is shown in the green spectrum.

defined, $\frac{A_{\text{Derivative}}}{A_{\text{Template}}} = \text{DTR}$, $\frac{A_{\text{Derivative}}}{A_{\text{Filter}}} = \text{DFR}$, $\frac{A_{\text{Derivative}}}{A_{\text{Integral}}} = \text{DIR}$, $\frac{A_{\text{Template}}}{A_{\text{Filter}}} = \text{TFR}$, $\frac{A_{\text{Template}}}{A_{\text{Integral}}} = \text{TIR}$ and $\frac{A_{\text{Filter}}}{A_{\text{Integral}}} = \text{FIR}$. By calibration, these ratios are set to one for events caused by the decay of ^{163}Ho (compare to Figure 5). Further, in the scatter plots of these ratios, ^{163}Ho induced events are located inside of ellipses located at $\text{ratio}_a \approx \text{ratio}_b \approx 1$ (compare to Figure 6).

The contours of the densities are elliptical or symmetrical shaped for the innermost, densest contours (compare to red region) and are oval or asymmetrical shaped for less dense regions (orange to blue region). The asymmetric shape is due to the presence of different families

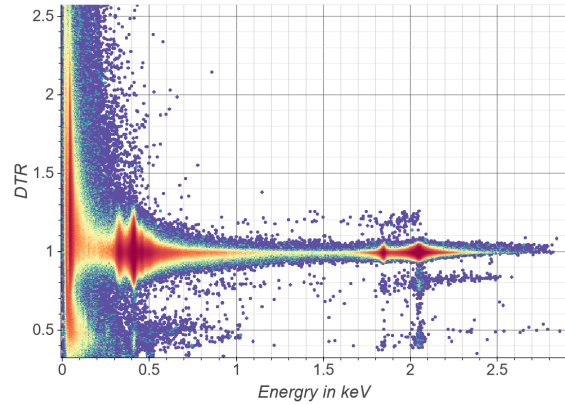


Fig. 5: DTR parameter against the deposited Energy of events of ^{163}Ho -loaded pixels. The ^{163}Ho lines can be observed around $\text{DTR} \approx 1$.

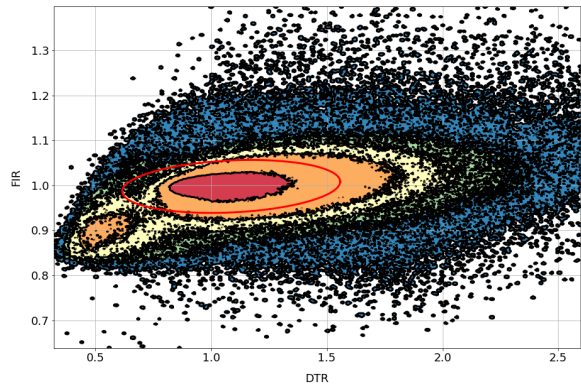


Fig. 6: FIR parameter against DTR parameter of events of ^{163}Ho -loaded pixels. The contours of the density of the events are shown. The ^{163}Ho induced events are located in an ellipse around $\text{FIR} \approx \text{DTR} \approx 1$. The fitted ellipse is shown in red.

of pulses. ^{163}Ho caused events are mainly located in the innermost region, thus The minor and major axis of the ellipses can be obtained by fitting an ellipse to the contour of the densest part of the scatter plots (red region). The scale of the ellipses can be obtained by using the χ^2 distribution of the events corresponding to the energies of ^{163}Ho MI, MII, NI and OI lines located inside the ellipses. For different scales a χ^2 distribution is fitted to the χ^2 distribution of the data points and the sum of the squared residuals is calculated each. The summed squared residuals have a well defined minimum for a certain scale (see Figure 7), which defines the scale for the ellipse and is determined by fitting a β distribution. This is done for 3 parameter space separately, DTR-FIR, DFR-TIR and DIR-TFR. The condition that the events have to be located in every of the three ellipses

can be defined. The events fulfilling both conditions, the non-coincidence and the ellipse condition are shown as the green spectrum in Figure 4. Using the ellipse conditions, the fraction of events with larger χ^2 and the bump on the right side of the peak is reduced.

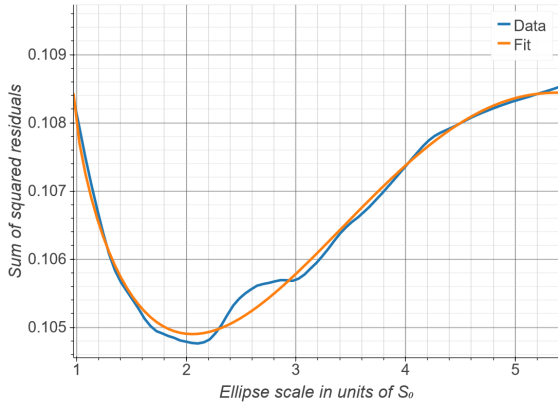


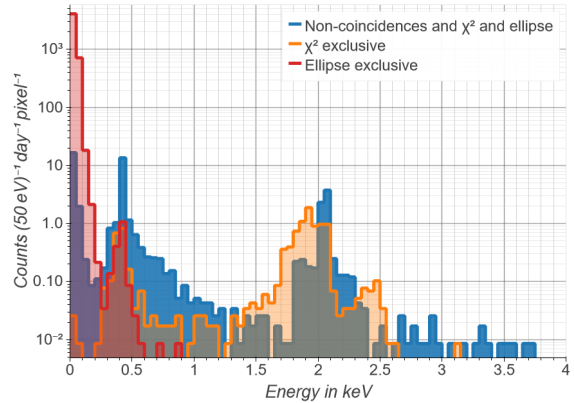
Fig. 7: The sum of squared residuals for different ellipse scales. S_0 is the diameter of the ellipse fitted to the densest part of the energy ratio - energy ratio parameter room. The shape is fitted by a β distribution to determine the position of the minimum.

1.3 Event classification

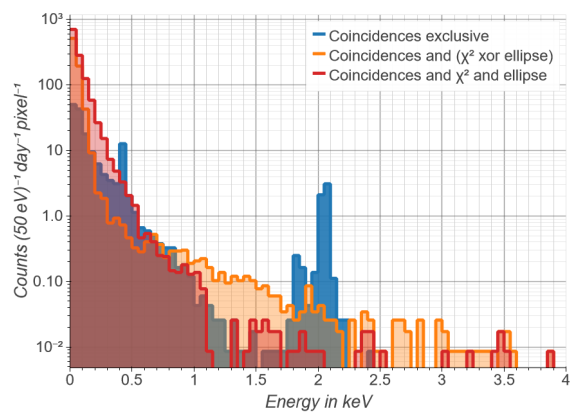
With each set of cut conditions, different classes of pulses can be chosen. The energy spectra of removed events recognized by different combinations of cuts are shown in Figure 8.

Phone signals

Most of the removed low energy pulses ($E < 500$ eV) are most likely caused by the 1.8 MHz frequency band of Global System for Mobile Communications (GSM) phone signals. Two pixels are readout by the same SQUID and raise signals with inverted polarity in respect of each other. Thus, if one of both pixels raises a signal and the other pixel raises a signal after about $550 \mu\text{s} \approx \frac{1}{1800 \text{ MHz}}$ triangular or rectangular pulse shapes result, depending on the pulse height ratio of the two signals (see Figure 9). These events are either cut exclusively by the ellipse cut (red spectra of Figure 8a) or by the coincidence cut combined with at least one other cut (red and orange spectra of Figure 8b). In case of events recognized exclusively by the ellipse cut, these pulses have a triangular shape. The peak around the energy of the ^{163}Ho N-lines could be caused by coincidences of the decay ^{163}Ho with a phone signal. For higher energies, the



(a)



(b)

Fig. 8: Spectrum of deposited energies of removed data of the ^{163}Ho -loaded pixels. **a)** The blue spectrum corresponds to events exclusively cut with the χ^2 and ellipse cuts. The orange spectrum corresponds to data exclusively recognized by the χ^2 cut. The red spectrum consists data exclusively removed by the ellipse cut. **b)** The blue spectrum corresponds to events exclusively cut by the coincidence cut. The orange spectrum corresponds to data exclusively recognized by the coincidence cut and exactly by one of the other two cuts. The red spectrum consists data removed by all three cuts.

amplitude of the phone signal on top of the ^{163}Ho signal could be relatively low compared to the actually signal amplitude. Thus, the variation of the pulse shape could be minor affected at higher energies and could be unrecognized. This type of energy dependency should be negligible, since only 10^{-4} of all ^{163}Ho N-line events are cut by the ellipse cut exclusively. Further, no events in the endpoint region of ^{163}Ho EC decay of about 2.8 keV are exclusively cut by the ellipse cut.

In case of GSM events recognized also by the coincidence cut the distribution of the coincidence multiplicity, the number of pixels raising simultaneously a signal,

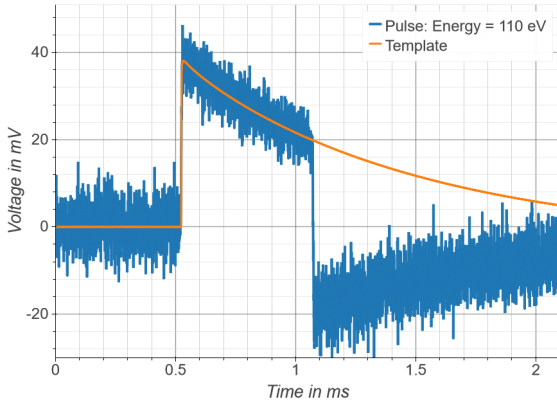


Fig. 9: Pulse removed by the coincidence and exactly one of the other cuts. About $550 \mu\text{s}$ after the raise of the pulse, the other pixel of the same read out channel and with inverted polarity raises a signal.

is almost uniform distributed for multiplicities of three to 13 and decreases to higher values (see Figure 10). A multiplicity of x means that x events are coincidental to the given event.

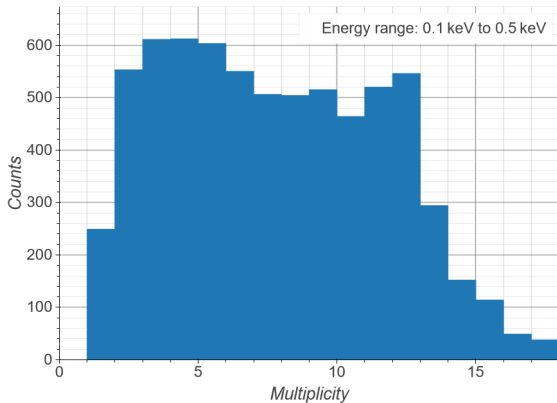


Fig. 10: Distribution of coincidence multiplicities of events recognized by the coincidence and by exclusive one other cut. A value of x means that $x + 1$ pixels raise simultaneously a signal.

Substrate heating

The distribution of multiplicities is different for pulses corresponding to higher energies ($E > 500 \text{ eV}$). For events cut by all three cuts (red spectrum of Figure 8b), high multiplicity values are preferred (compare to Figure 11). These pulses have longer decay times compared to events caused by the decay of ^{163}Ho and roundings of the maxima (Figure 12). The rise of the thermal pulses is limited by the coupling of the conducting electron

system of the detector to the spin system of the sensors [2]. However, for the discussed data the rise of the time profile pulses are limited by the bandwidth of the readout electronics [3]. The decay time of the pulses is given in first order by the thermal coupling of the sensors to the thermalization structures. Considering a charged particles traveling through the absorber, sensor and substrate, energy can be transferred to the spin system on different time scales resulting in modifications of the pulse shape compared to pulses caused by the decay of ^{163}Ho in the absorbers. Events with $E > 500 \text{ eV}$ and which are recognized by all three cuts show both, a longer rise time and a longer decay time. Combined with the high coincidence multiplicity, we can assume that this type of events are caused due to heating of the whole substrate.

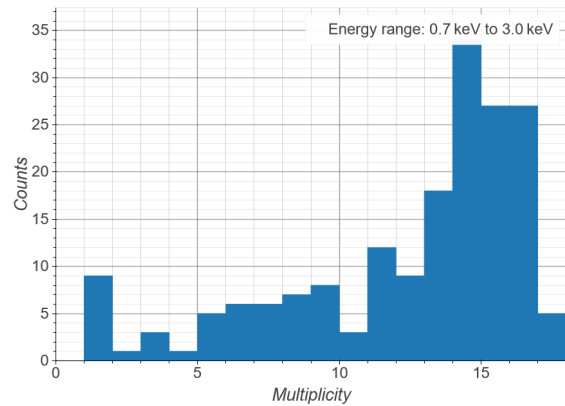


Fig. 11: Distribution of coincidence multiplicities of events cut by all three cuts. A value of x means that $x + 1$ pixels raise simultaneously a signal.

Particle generated signals

In case of events corresponding to energies $E > 500 \text{ eV}$, which are recognized by the coincidence cut and by exactly one of the other two cuts (orange spectrum of Figure 8b), the spectrum of multiplicities does not peak at high multiplicities, but at low (Figure 13). These pulses have also longer decay times compared to the pulses caused by the decay of ^{163}Ho , but they have in addition a spiky maximum (Figure 14). These kind of events could be caused by particle hitting a certain region of the detector chip. With this, the substrate could be heated only locally, what could explain the longer decay time of the pulses. The rise time is shorter than the rise time of pulses caused by the ^{163}Ho decay. This could be explained by particles passing through the absorber and sensor of a MMC. This could also explain the spiky maximum of the pulses, which could be caused

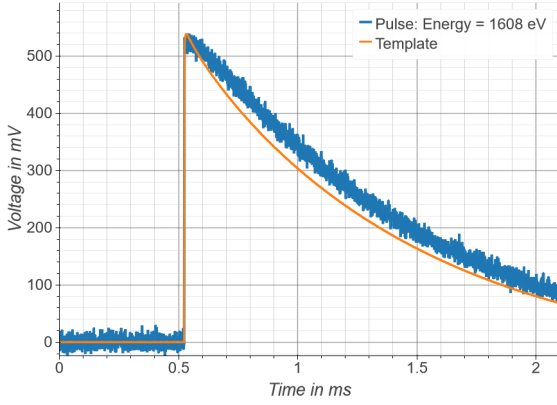


Fig. 12: Time trace of an event recognized by all three cuts. The decay time of the pulse is longer compared to the template pulse.

by energy deposited directly in the sensor and coupling directly with the spin system. These events can also be found in the spectrum of events cut exclusively by the coincidence cut (blue spectrum of Figure 8b). But, these events have multiplicities of about 10 and the energies are mostly lower ($E < 500$ eV).

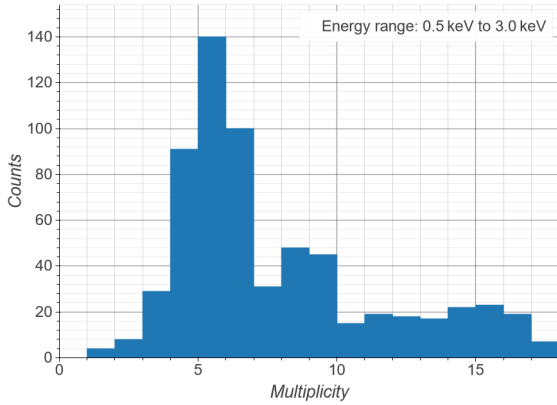


Fig. 13: Distribution of coincidence multiplicities of events recognized by the coincidence at exactly one other cut. A value of x means that $x + 1$ pixels raise simultaneously a signal.

Pulses with spiky maximums and short rise times can also be identified with the χ^2 cut (orange spectrum of Figure 8a). In contrast to the previous pulse family, these pulses show the same decay time than pulses due to the ^{163}Ho decay. If these pulses are caused by particles passing through the absorbers, the particles could be stopped in the sensors and thus, the decay time is not affected. Moreover, with this explanation the absence

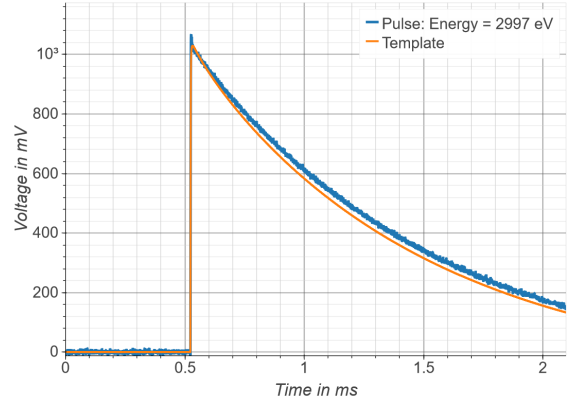


Fig. 14: Time trace of an event cut by the coincidence and exactly one other cut. The decay time of the pulse is longer compared to the template pulse. Also, a spike is on top of the maximum of the pulse.

of coincidences could be explained, because no energy is deposited in the substrate.

Miscellaneous

Pile-up events can be recognized by either the χ^2 , ellipse or the combination of both cuts (all three spectra of Figure 8a).

Events, corresponding to the ^{163}Ho lines, exclusively recognized by the coincidence condition (blue spectrum of Figure 8b) are random coincidences. The multiplicity of these events is exactly one. Also, the intensities of the lines are in good agreement with the expected spectrum of random coincidences for the given time window and 0.3 Bq of ^{163}Ho per pixel.

1.4 Energy dependency of cuts

The cut efficiency of the coincidence cut is by definition energy independent for ^{163}Ho induced events. Only the trigger time is considered. In contrast, the reduced χ^2 is scattered for ^{163}Ho induced events for the same energies (compare to Figure 2), but it is similar distributed for different energies ($E > 200$ eV). Thus, the cut efficiency of the χ^2 cut should also be the same for all energies for ^{163}Ho induced events [4]. The ratios of the reconstructed energies are different distributed for different energies (see Figure 5). Thus, more ^{163}Ho induced events with low energies could be removed than events with higher energies. However, it was shown in the previous Chapter 1.3 that only about 10^{-4} of all events with energies similar to the energy of the ^{163}Ho N-line were removed. These events show different pulse shape than ^{163}Ho induced events and are probably caused due to pile-up of the ^{163}Ho decay and phone signals. We can

assume that similar events occur also at higher energies and are not recognized. But this should only be a very tiny fraction ($< 10^{-4}$) of all events. The events located outside of at least one ellipse differ strongly from the events located in all ellipses, by comparing the distribution of the decay times¹ of the pulses with $\chi^2 \text{dof}^{-1} < 2$ (Figure 15). Pulses inside the ellipses have mostly a decay time of about 0.8 ms and pulses outside of at least one ellipse less.

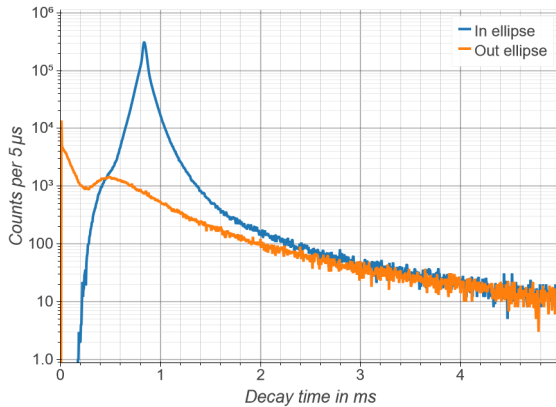


Fig. 15: Spectrum of the decay times of pulses with $\chi^2 \text{dof}^{-1} < 2$. The blue spectrum shows pulses located inside all ellipses. The orange spectrum contains pulses, which are at least outside of one ellipse. The pulses inside the ellipses have mostly a decay time of 0.8 ms, the other pulses less.

References

1. A. Göggelmann, et al., *The European Physical Journal C* **81**, 363 (2021). DOI 10.1140/epjc/s10052-021-09148-y. URL <https://doi.org/10.1140/epjc/s10052-021-09148-y>
2. S.R. Bandler, et al., *Journal of Low Temperature Physics* **93**(3), 709 (1993). DOI 10.1007/BF00693500. URL <https://doi.org/10.1007/BF00693500>
3. F. Mantegazzini, et al., *Journal of Instrumentation* **16**(08), P08003 (2021). DOI 10.1088/1748-0221/16/08/p08003. URL <http://dx.doi.org/10.1088/1748-0221/16/08/P08003>
4. R. Hammann, et al. Data reduction for a calorimetrically measured ^{163}Ho spectrum of the ECHo-1k experiment (2021)

¹The decay of the pulses can be described by an exponential function.

Danksagung

Ohne die tatkräftige Unterstützung einiger Personen wäre ich nicht in der Lage gewesen, diese Arbeit innerhalb einer endlichen Zeitspanne zu Ende zu bringen. Diesen Personen möchte ich im Folgenden herzlichst danken.

Ohne meine beiden Betreuer Prof. Dr. Josef Jochum und JProf. Dr. Loredana Gastaldo wäre diese Arbeit gar nicht erst zustande gekommen, weshalb ich mich bei beiden bedanken möchte, mir diese spannende Arbeit ermöglicht zu haben. Im regen Austausch mit ihnen habe ich viel gelernt und eine äußerst gute Betreuung erfahren.

Die freundschaftliche Atmosphäre an der PIT kam dank der gesamten Gruppe zustande, welche immer ein offenes Ohr für sämtliche Probleme hatte. Insbesondere danke ich Dr. Christian Strandhagen, auf welchen ich mich stets verlassen konnte und der mir oft mit Rat zur Seite stand, wenn Fragen zur Physik oder zur Programmierung auftauchten.

Dank der gesamten ECHO-Kollaboration konnte dieses spannende Experiment erst durchgeführt werden. Insbesondere möchte ich mich hier bei meinen Kollegen aus Heidelberg bedanken, zu welchen ein reger Austausch bestand.

Die Arbeit an der Dissertation war teilweise zeitlich und geistig sehr fordernd. Auf Stephanie, Isabella und Jonathan konnte ich mich stets verlassen, sie waren und sind immer für mich da.

Der DFG gilt Dank, da sie die finanziellen Mittel für dieses Projekt bereitstellte.